RADIOMETRIC ANALYSIS

OF THE LONGWAVE INFRARED CHANNEL

OF THE THEMATIC MAPPER ON LANDSAT 4 AND 5

RIT/DIRS Report #86/87-51-112

Prepared by

John R. Schott
William J. Volchok
Joseph D. Biegel

Digital Imaging and Remote Sensing Laboratory

Center for Imaging Science

Rochester Institute of Technology
One Lomb Memorial Drive
Rochester, New York 14623

TABLE OF CONTENTS

Section	Title	Page

ACKNOWLEDGEMENTS

List of Figures

List of Tables

SECTION I

Introduction and Summary

This document reports on the results of a study with a two-fold purpose. The first objective was to evaluate the postlaunch radiometric calibration of the Landsat Thematic Mapper (TM) band 6 data. The second objective was to determine to what extent surface temperatures could be computed from the TM band 6 data using atmospheric propagation models. To accomplish this, ground truth data were compared to a single TM-4 band 6 data set. This comparison indicated satisfactory agreement over a narrow temperature range. However, systematic errors were apparent which could not be adequately evaluated using only the available ground truth data. Subsequently thermal infrared line scanner missions were flown under the satellite on 6/22/1984, 10/6/1984 and 5/24/85 in the vicinity of Rochester, NY. The underflight data permit direct measurement of surface temperature over large areas for direct correlation with the spacecraft data. In addition, the underflight data can be used to measure atmospheric effects for comparison to the atmospheric propagation models.

The atmospheric propagation model (modified LOWTRAN 5A) was used to predict surface temperature values based on the radiance at the spacecraft. The aircraft data were calibrated using a multi-altitude profile calibration technique which had been extensively tested in previous studies. This aircraft calibration permitted measurement of surface temperatures based on the radiance reaching the aircraft. When these temperature values are evaluated, an error in the satellite's ability to predict surface temperatures can be estimated. This study indicated that by carefully accounting for various sensor calibration and atmospheric propagation effects, the expected error (1 standard deviation) in surface temperature would be 0.90°K. This assumes no error in surface emissivity and no sampling error due to target location.

These results indicate that the satellite calibration is within nominal limits to within this study's ability to measure error. There is some minor concern that the apparent gain of the system may be higher than the nominal values, however, those errors are smaller than detectable by this method.

In addition to the definition and testing of the calibration method a procedure for generation of surface temperature images has been identified and demonstrated. This method uses the radiometric calibration and atmospheric propagation methods

1

coupled with emissivity lookup tables accessed by land cover to compute blackbody equivalent surface radiance or the corresponding kinetic temperature. The land cover type can be derived by multispectral classification of the short wavelength spectral channels on the TM. The resultant "temperature" images can be readily interpreted as they appear to have higher resolution than the originals. While this is only an artifact of the processing, it can improve interpretation and temperature values can be directly evaluated from the images for targets significantly larger than the TM-6 projected pixel size.

SECTION II

Technical Approach

This Section contains a review of the relevant literature and a discussion of the radiometry governing calibration of satellite systems. Based on this background, the approaches used for collection and analysis of the satellite, aerial and surface truth data are presented.

2.A Literature Review

The data from the thermal infrared channel (Band 6) aboard the thematic mapper represents the highest spatial resolution thermal information yet available from space. The radiometric response function of the thermal sensor had to be carefully evaluated after launch to permit proper interpretation of these unique data. Probably the most generally accepted method for processing radiometric data from space is to correct the observed radiance or apparent temperature to a surface radiance or temperature value using atmospheric propagation models. For example, using radiosonde data from the study area at the time of an overpass the atmospheric transmission and path radiance terms (τ and L_u) can be computed using AFCRL's LOWTRAN code (Selby, et al. 1978). These terms can be used to compute the surface radiance from

$$L_T = (L - L_u)/\tau. \qquad\qquad (2.A-1)$$

where; L is the observed radiance and L_T is the surface radiance which can be associated with an equivalent blackbody temperature (T).

As part of NASA's Heat Capacity Mapping Mission (HCMM) experiment atmospheric propagation models were used in reverse in an attempt to evaluate the post launch radiometric response of the Heat Capacity Mapping Radiometer (HCMR). Bohse et al. 1979, describe how surface radiometric readings were used in conjunction with radiosonde data to predict the radiance at the top of the atmosphere using atmospheric propagation models. Surface data taken with a point radiometer viewing a lake were averaged to define L_T and the atmospheric propagation models were used to define τ and L_u at the time of the satellite overpass. Therefore, the radiance observed by the spacecraft sensor L' and the radiance calculated from the model ($L = \tau L_T + L_u$) should be identical. In fact for the five dates studied, the difference in observed and predicted values ranged from 4.15 to 6.14°C with an average difference of 5.24°C (radiance values have been converted to equivalent blackbody temperatures).

3

As a result of these analyses, NASA offset the prelaunch calibration values for the sensor by -5.5°C and applied this offset to all standard HCMM products (c.f. HCMM users guide). It should be noted that these single point readings provide almost no data on system gain and all error had to be attributed to bias.

This offset was based on the assumption that the sensor response and/or the calibration standard had somehow changed since the prelaunch calibration. Subsequent studies five months later conducted in an identical fashion indicated that the offset should be moved back toward the original value by 3.3 to 7.7°C (Subbarayudu 1979). This would essentially nullify the original offset. If we accept the initial premise of a shift in the HCMR response function, we must now speculate on the possibility of long term drift in the sensor calibration. An alternative and perhaps more acceptable hypothesis is that the atmospheric propagation models are inadequate and part or all of the variance is associated with changes in the atmosphere insufficiently accounted for by the models.

Whether the sensor or the models were at fault — the fact remains that — the radiometric calibration of the data was seriously in question. To minimize this type of concern regarding the thermal data from Landsat 4 and 5, the radiometric response function of the sensor was carefully evaluated after launch using reliable experimental data. Since nearly all users have a requirement for surface radiance data, it was also essential that the atmospheric propagation models be more carefully evaluated and refined as preprocessing algorithms. Without reliable atmospheric propagation models, costly field experiments would be required as part of each image analysis effort.

The preliminary analysis of TM band 6 data also further emphasized the need for more detailed assessment of post launch calibration and refinement of atmospheric propagation models. Malaret et al. 1985 report observing nearly the same apparent temperature range at the satellite as observed on the ground. Similar results were reported by Wukelic et al. 1975. Wukelic goes on to report that use of the atmospheric propagation model tended to degrade the correlation between satellite predicted temperature and surface temperature. These data tend to indicate that either the atmosphere is exhibiting negligible attenuation or that the sensors post launch gain had somehow increased and that this increase had not been accounted for during internal calibration. While atmospheric transmission is difficult to know exactly, general patterns are well defined and transmissions of the order of 0.75 to 0.90 might be expected. Transmission values

4

in this range make the results reported by these investigators unlikely. The problems of atmospheric propagation models, adequate ground truth and post launch calibration must all be addressed in order to properly assess Landsat TM band 6 data. We should point out that the surface temperatures used for the previously sited analyses are all point samples generally taken as grab samples which may not adequtely represent surface temperatures over large regions (e.g. the approximately 57,600m^2 region of uniform temperature necessary for good TM6 ground truth). In order to adequately address some of these questions, we need to consider the work done on atmospheric modeling, measurement of atmospheric parameters and the potential for viable ground truth assessment.

Schott 1979 (c.f. Appendix A) describes an empirical method for computation of atmospheric transmission and upwelled path radiance. The method involves flying an infrared line scanner at a series of altitudes over the same targets. The method was demonstrated to permit measurement of water surface temperatures to within 0.4K of actual surface temperatures in a series of blindfold tests. Schott and Schimminger 1981 subsequently used this approach to calibrate NASA's HCMM longwave infrared (LWIR) satellite. In this study the aerial infrared imager was flown in conjunction with a satellite overpass. The aerial data were calibrated using the method of Schott 1979 and large regions of uniform temperature were identified and measured. Because of the well documented accuracy of the aerial calibration method, these regions could be used as calibration points for the satellite. Satellite observed radiance values could then be converted to surface temperatures using regression models of satellite radiance versus surface radiance.

Subsequently Schott and Biegel 1983 and Byrnes and Schott 1986 utilized the multiple altitude calibration method to compare empirically derived atmospheric calibration parameters to those derived from the LOWTRAN model. They demonstrated that the LOWTRAN 5A model could be evaluated using this approach and that for low altitude work a modified version of LOWTRAN could be brought into reasonable agreement with empirical studies. At higher altitudes some discrepancies still exist requiring further refinement to the LOWTRAN model.

The study reported here was designed to draw on these previous efforts. Underflight data were used to generate ground truth to calibrate the sensor, LOWTRAN models and underflight data were compared to assess the feasibility of calibrating the sensor to ground temperature using atmospheric propagation models.

5

Finally, the potential for using the reflected TM bands to assist in analysis of thermal TM data was evaluated.

2.B Theoretical Background

This section will review the relevant TM band 6 sensor characteristics and the radiation propagation physics relevant to the evaluation and calibration of the LWIR sensor for earth surface temperature assessment.

2.B.1 Thematic Mapper

The Thematic Mapper's operating principles and performance are extensively discussed in Markham and Barker 1985 and Barker 1985. Only brief review of relevant material related to TM band 6 will be presented here. The TM optical train is presented in Figure 2.B-1. The 170 μ radian angular IFOV of the 4 mercury cadmium teleride detectors projected onto the ground from the 705 km nominal altitude yields a spot size of 120 meters. Four lines of data are collected by the four sensors with each ocillation of the scan mirror. Radiometric calibration of the LWIR channel is accomplished during the scan mirror turn around time. A shutter cycles into the optical train immediately behind the the primary mirror. The shutter is thermally controlled and is used to provide a reference radiance, as well as for DC restoration. In addition, a small concave mirror on the shutter surface reflects a thermally controlled blackbody into the detector field of view for a brief period during each scan reversal. Thus, a two point radiance calibration is acquired for each scan line. (A more detailed discussion of sensor calibration is contained in Section 2.D). The spectral response of the LWIR sensors is shown in Figure 2.B-2. Through internal calibration of the LWIR sensor the within band radiance [$wcm^{-2}sr^{-1}$] or the effective mean spectral radiance [$wcm^{-2}sr^{-1}\mu m^{-1}$] can be generated from the digital count recorded at each image location. This is accomplished through a simple linear relationship between the observed signals for the shutter and the blackbody with the known radiance values. These signals are then linearly scaled to digital counts to set the minimum and maximum digital counts at prescribed radiance levels.

Thus, in the discussions which follow we will assume the radiance reaching the satellite sensor is known (i.e. can be determined from digital count) and proceed with a discussion of what processes and parameters contribute to the radiance reaching the sensor.

6

SCAN LINE CORRECTION

COOLED DETECTORS AND FILTERS

BANDS 5 6 7

SILICON DETECTORS AND FILTERS

BANDS 1 2 3 4

SCAN MIRROR

ALONG TRACK DIRECTION

ORBIT DIRECTION

SWATH WIDTH 185 km

TM DETECTOR DETAILS

BANDS

1 2 3 4 5 7   6

SCAN DIRECTION

GROUND IFOV
BANDS 1–5 & 7   30 METERS
BAND 6   120 METERS

DATA RATE — 84.9 MBPS
QUANTIZATION LEVELS — 256
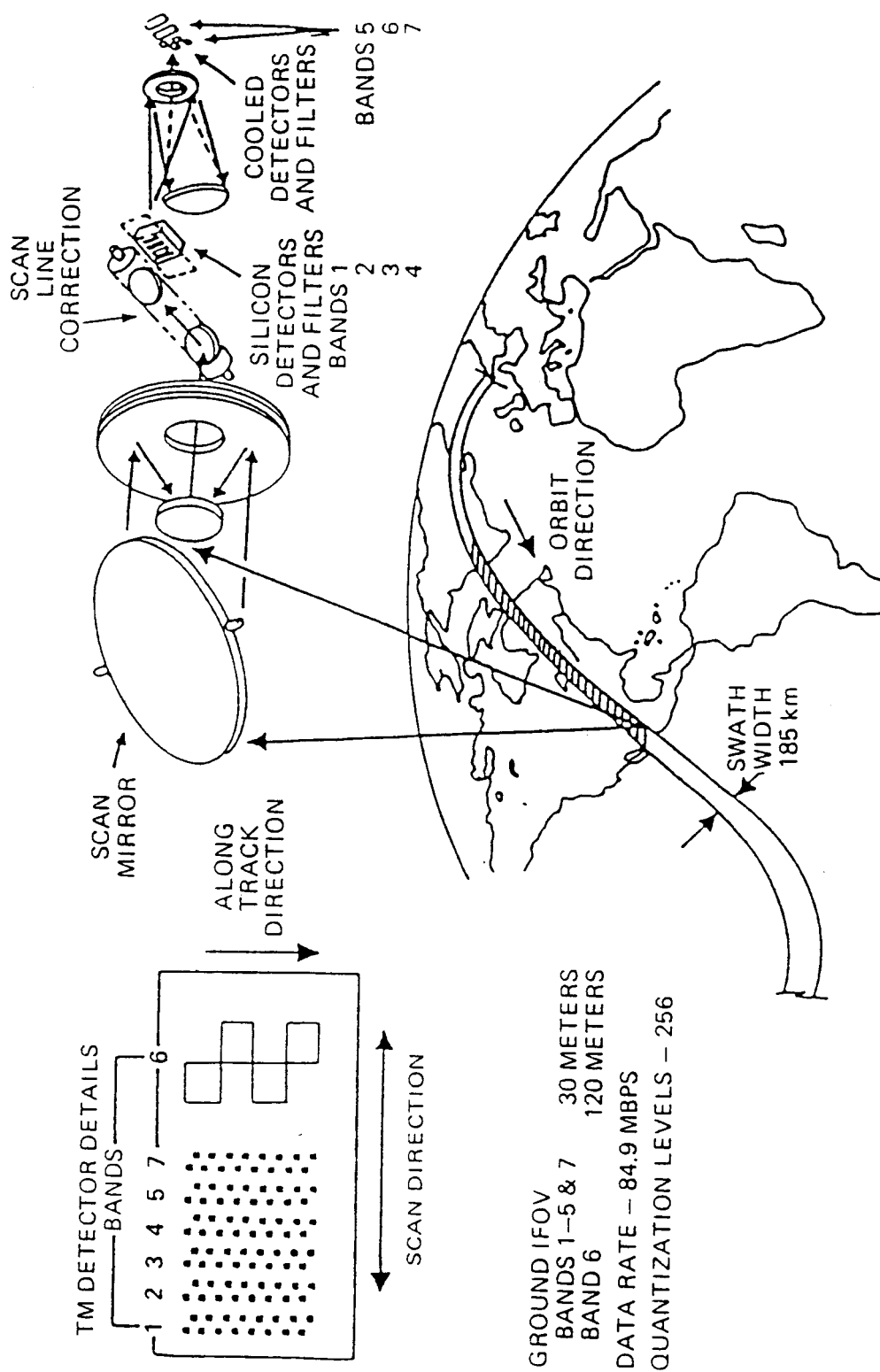
2.B-1   Schematic of the Thematic Mapper [from Irons 1985]

7

Detector 1 · Detector 2 · Detector 3 · Detector 4

(Each plot: Relative Spectral Response, RSR vs Wavelength (Micrometers), with PROTO-FLIGHT and FLIGHT curves)
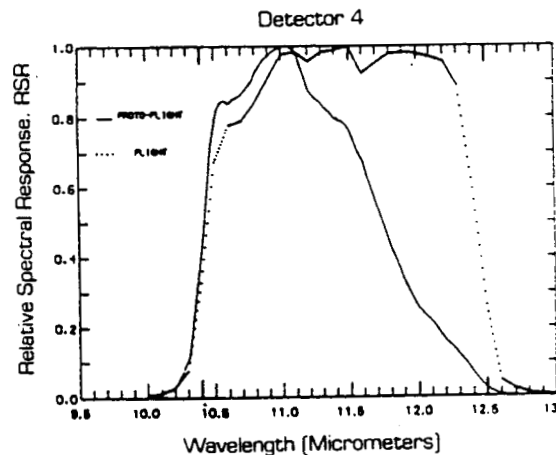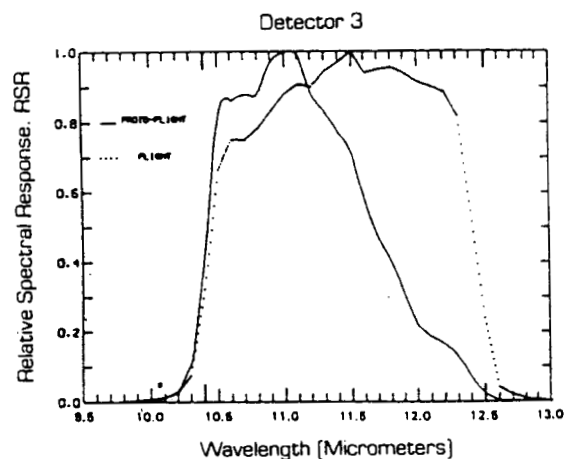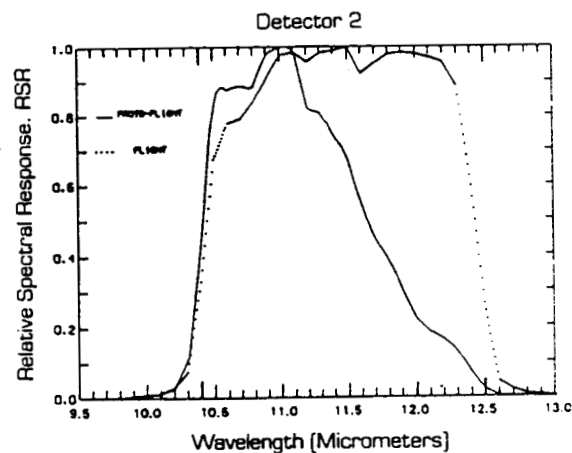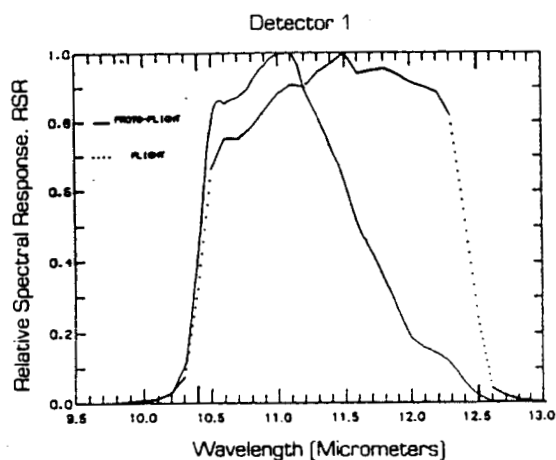
Spectral Parameter	Specification	TM4 Proto-Flight	TM5 Flight
LOWER BAND EDGE (μm)	10.4 ± 0.1	10.42	10.45
UPPER BAND EDGE (μm)	12.5 ± 0.1	11.66 *	12.43
LOWER BAND EDGE SLOPE (μm) 5% TO 75%	0.3 (MAX)	0.25	0.34 *
UPPER BAND EDGE SLOPE (μm) 75% TO 5%	0.3 (MAX)	1.01 *	0.26
FLATNESS (%)	75	67 *	78

*OUT OF SPECIFICATION

2.B-2 Thematic Mapper Spectral Performance—Band 6

8

(From Markham and Barker 1985)

2.B.2 Governing Equations

In this section we will describe the atmospheric propagation model used to describe and simulate the radiance reaching both airborne and satellite LWIR imaging sensors. Included in this section is a description of a model for computation of atmospheric and target interaction effects on the radiance or apparent temperature perceived by an airborne or satellite sensor. In addition, procedural methods to exercise the model and compare it to empirical data are presented.

In the simplest case, let the radiance reaching a sensing platform be

$$L = \tau \epsilon L_T + L_u + r L_D \tau \qquad (2.B-1)$$

where τ is the atmospheric transmission, ϵ is the emissivity of the target, L_T is the blackbody radiance associated with the target's kinetic temperature (T), r is the reflectivity of the target, L_D is the downwelled radiance from the hemisphere above the target (note the implicit Lambertian assumptions) and L_u is the upwelled radiance or path radiance reaching the sensor from the atmospheric path. Each term in Equation 2.B-1 is wavelength dependent and governed by the spectral bandpass of the sensing system. For example,

$$L_T = 2hc^2 \lambda^{-5} \int_{\lambda_1}^{\lambda_2} (e^{-hc/\lambda kT} -1)^{-1} \, d\lambda \qquad (2.B-2)$$

where h is Plank's constant, c is the speed of light, λ is wavelength, λ_1 and λ_2 are the spectral bandpass limits of the sensor, k is the Boltzmann constant, and T is the kinetic temperature. Note that for convenience we have assumed that all of the parameters in Equation 2.B-1 are slowly varying functions of wavelength so that they can be taken outside the wavelength integral for small passbands.

Equation 2.B-1 (illustrated in Figure 2.B-3) can be expanded to explicitly incorporate the dependence of the observed radiance on altitude (h) and view angle (Θ). In this case

$$L (h,\Theta) = \tau(h,\Theta) \, \epsilon (\Theta) \, L_T + L_u(h,\Theta) + r(\Theta) \, L_D \, \tau (h,\Theta) \qquad (2.B-3)$$

The term $r(\Theta)$ should more properly be expressed as a scattering function incorporating the contributions from each segment of the hemisphere above the

9

L_U

rL_D'

$\varepsilon L_T'$

ORIGINAL PAGE IS
OF POOR QUALITY

$L_D(\theta_i)$

εL_T

target reflected into the acceptance angle of the sensor. However, because this scattering function is undefined for most surfaces of interest, we have assumed the surfaces are either perfectly diffuse, i.e., $r(\theta) = r(0)$ or that the scattering function is independent of azimuth angle and only varies as a function of view angle. These restrictions can easily be removed for surfaces whose scattering functions are more fully defined with respect to azimuthal angles. To implement a model described by Equation 2.B-3 each term on the right hand side must be defined. Each term is treated separately in the discussion which follows with the combined process illustrated in Figure 2.B-4.

The model described in more detail in Schott 1983 uses the LOWTRAN 5A computer code to generate within band transmission values as a function of altitude over the bandpass of interest. These values are derived within LOWTRAN from radiosonde measurements of the atmospheric makeup (input to LOWTRAN) and stored data based on empirical measurements that relate optical depth and hence transmission to the atmospheric composition.

Rather than run LOWTRAN's spectral computation for each sample, the bandpass values for several altitudes are stored in the current model and interpolated in a log linear fashion to any input altitude. The increase in optical depth due to viewing along a slant path is computed by the present model and transmission values are derived based on the LOWTRAN relationships between transmission and optical depth.

The emissivity as a function of view angle must be stored as a data array in the model for each object of interest. Unknown points are found as a function of view angle by interpolation. For the data sets reported here, all viewing is considered vertical so variation in emissivity with view angle can be neglected. The reflectivity is obtained from the emissivity by employing Kirchoff's rule $r(\theta) = 1 - \varepsilon(\theta)$.

The blackbody equivalent radiance associated with a temperature T or the apparent temperature associated with a radiance value is found by interpolation of a radiance-temperature array generated by numerical integration of the Plank equation (Equation 2.B-2).

The upwelled radiance at any angle (θ) and altitude (h) is computed from

11

Atmospheric Inputs
T = f (h) From Lowtran
T = f (h) From Radiosonde

Target Inputs
h, θ, T
$\varepsilon = f(\theta)$

Transmission To Altitude h
Interpolated From Lowtran
Transmission

Slant Path
To Target

Increase In
Optical Depth

Correction To Vertical
Transmission For Slant
Path $\tau(h, \theta)$

$\varepsilon(\theta)$ & $r(\theta)$
By Interpolation Of
$\varepsilon = f(\theta)$

L_T From Radiance Temp
Lookup Table

$\tau(h, \theta)\ \varepsilon(\theta)\ L_T$

Source
Term

Contribution To
Path Radiance
From Each Layer

Σ

Path Radiance to
Altitude h Through
View Angle θ

$L_U\ (h, \theta)$

Path
Radiance
Term

Contribution To
Downwelled
Radiance From
Each Layer

Σ

$L_D(\theta)$ Path Radiance
Contribution From
Each Angle

$\int_\Omega$

$L_D\ r(\theta)\ \tau(h, \theta)$

Reflected
Radiance
From
Skydome

Observe
Radiance L

T, Apparent Temp
From Radiance—
Temperature Lookup

2.B-4   Atmospheric Propagation Model

$$L_u(h,\theta) = \sum_{i=1}^{n} L_{T_i} [1 - \tau_i (h_i,\theta)]\tau_j(h_i,\theta) \qquad (2.B-4)$$

where n is the number of homogeneous layers between the source and the sensor into which the atmosphere is assumed to be divided (typically preselected at 20), i defines the atmospheric layer considered, L_{T_i} is the radiance associated with the mean temperature of the layer (T_i), (the mean temperature of the layer is found by interpolation of the radiosonde altitude vs. temperature data which is included as a data array), $\tau_i (h_i,\theta)$ is the transmission along the slant path through the ith layer having vertical height $h_i = h/n$, and $\tau_j (h_i,\theta)$ is the transmission along the slant path from the top of the ith layer to the sensor. The term $[1 - \tau_i (h_i,\theta)]$ can be thought of as the effective absorbtivity and therefore the effective emissivity of the ith layer when it is treated as a blackbody. This is the equivalent of assuming that the radiance scattered out of the layer is exactly replaced in magnitude and direction by the radiance scattered into the layer. Ben-Shalom et al., 1980 has suggested that this method represents an improvement over the LOWTRAN method for computation of path radiance. Figure 2.B-5 represents the process of summing the contributions from each layer in the atmosphere to obtain the cumulative path radiance $L_u(h,\theta)$.

The total downwelled radiance onto the target is computed from the contribution from each element of solid angle above the target. The downwelled radiance from any angle $L_D(\theta)$ is computed in a manner similar to that for upwelled radiance except the path length is always to space rather than to the sensor altitude. The irradiance on the target from the hemisphere above it can then be expressed as

$$E_D = \int L_D(\theta) \cos\theta \, d\Omega \qquad (2.B-5)$$

where the integral is on the solid angle Ω over the hemisphere above the target. It can be re-expressed in terms of an azimuth angle as shown in Figure 2.B-6 as

$$E_D = \int_{\phi=0}^{2\pi} \int_{\theta=0}^{\pi/2} L_D(\theta) \cos\theta \sin\theta \, d\theta d\phi$$

$$= 2\pi \int_{\theta=0}^{\pi/2} L_D(\theta)\cos\theta\sin\theta d\theta \qquad (2.B-6)$$

Assuming diffuse reflection from the surface the total downwelled radiance reflected can be expressed as

13

$$L_u$$

$$L_{T_i}$$

$$T_j$$

$$T_i$$
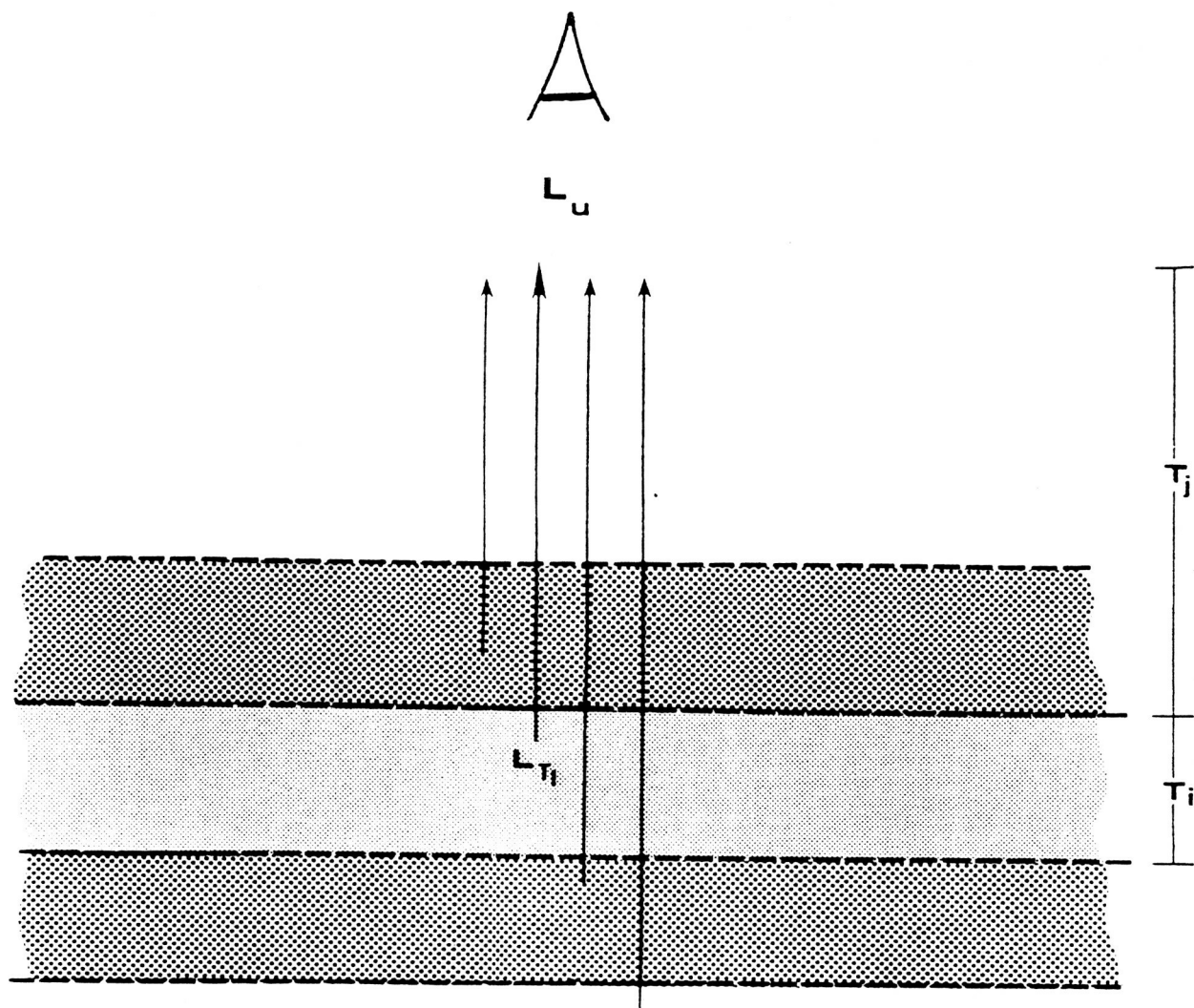
$$L_u = \sum_i L_{T_i} \cdot (1 - \tau_i) \cdot \tau_j$$

2.B-5   Summation of the Contributions from each Laser in the
         Atmosphere to Obtain the Cumulative Path Radiance
         Reaching a Sensor

14

$$r(\Theta)L_D = r(\Theta) E_D/\pi \tag{2.B-7}$$

The model described here computes the angular contribution to downwelled radiance $L_D(\Theta)$ in a manner similar to that described for the upwelled contribution to path radiance. A numerical integration of Equation 2.B-6 is then performed to arrive at a value for the irradiance incident on each target. Alternately, if the target is assumed to have purely specular reflection, the reflected radiance can be expressed as $r(\Theta) L_D(\Theta)$.

The reflectivity of the target is obtained by evaluating the emissivity vs. view angle array for each target type, where $r(\Theta) = 1 - \varepsilon(\Theta)$.

To this point we have not included the sensor's spectral response function. This is done within the LOWTRAN code by cascading the sensor spectral response function with the spectral radiance to yield a sensor weighted integrated radiance corresponding to the radiance sensed by the LWIR sensor, i.e.

$$L(h) = L_\beta(h) = \int_{\lambda_1}^{\lambda_2} L_\lambda(h)\beta_\lambda \, d\lambda \Big/ \int_{\lambda_1}^{\lambda_2} \beta_\lambda \, d\lambda \tag{2.B-8}$$

where $L(h) = L_\beta(h)$ is the sensor response weighted integrated radiance reaching the sensor (the subscript β will be assumed in all future discussions) $[\text{wcm}^{-2}\text{sr}^{-1}]$.

$L_\lambda(h)$ is the spectral radiance reaching the sensor as computed by the LOWTRAN code incorporating the Ben-Shalom 1980 modification $[\text{wcm}^{-2}\text{sr}^{-1}\mu\text{m}^{-1}]$.

β_λ is the relative spectral responsivity of the sensor (Markham and Barker, 1985a) and λ_1 and λ_2 are the passband limits of the sensor $[\mu\text{m}]$.

A method for computation of each parameter on the right hand side of Equation 2.B-3 has now been defined. To compute observed radiance at any altitude (AGL) and view angle the following inputs are required: the kinetic temperature of the surface, the emissivity of the surface as a function of view angle, the atmospheric transmission as a function of altitude (from LOWTRAN) and the atmospheric temperature as a function of altitude (from radiosonde data). Conversely the temperature of any point viewed from altitude (h) at view angle (Θ) can be computed from its observed radiance.

15

$$L_D = \left(\int_0 L_D(\theta) \cdot \cos\theta \cdot \sin\theta \, d\theta \, d\Phi \right) \Big/ \pi$$

2.B-6   Integration of Downwelled Radiance

16
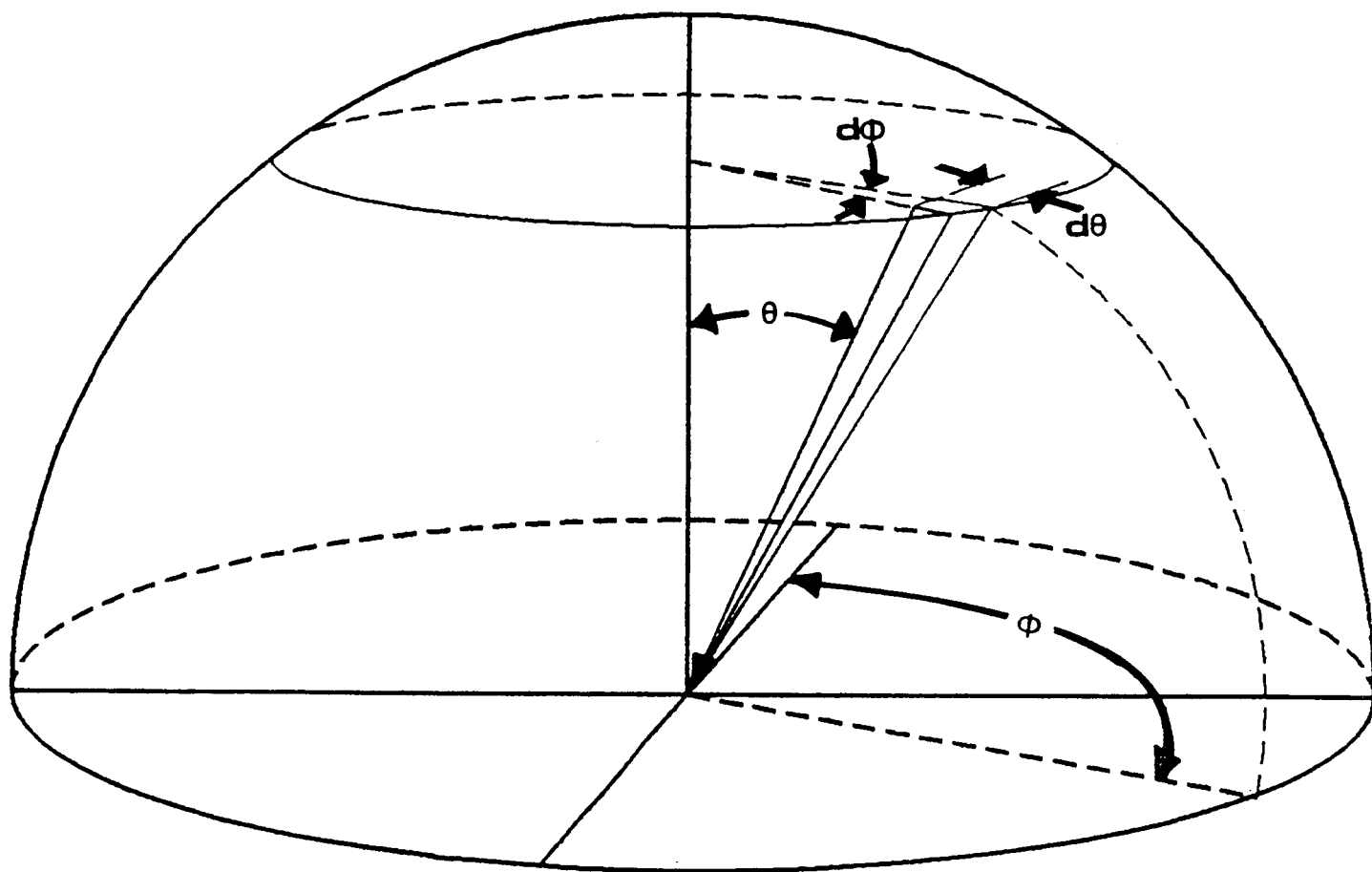
In the analysis which follows, this model was used to predict the radiance reaching the aircraft or satellite sensors. In addition, it was used in reverse to predict kinetic temperatures from observed radiance values.

2.B.3 Underflight Calibration Methods

Empirical data were collected using an airborne infrared line scanner. The scanner was filtered to limit the spectral bandpass to 8-14μm. (A narrow filter which attempted to match the TM sensor more precisely was also flown, but the reduced bandpass introduced serious noise problems). The use of an internal blackbody calibration system permits measurement of the observed radiance from the image records. This process is illustrated in Figure 2.B-7. This system permits measurement of the value L(h,Θ) in Equation 2.B-3 from thermal images.

Schott (1979) described an empirical procedure that uses radiance values observed at multiple altitudes over the same target to compute values of τ and L_u. For convenience, vertical viewing is assumed reducing Equation 2.B-3 to:

$$L_i(h,0) = \tau(h,0)L_i(0,0) + L_u(h,0) \tag{2.B-9}$$

where; $L_i(h,0)$ is the radiance observed vertically at altitude h for target i.
$\tau(h,0)$ is the vertical transmission from the earth to the sensor.
$L_i(0,0)$ is the radiance a sensor at the surface would observe from the ith target (i.e. $L_i(0,0) = \varepsilon(0)L_{Ti} + r(0)L_D)$.
$L_u(h,0)$ is the upwelled vertical path radiance to the sensor at altitude h.

By observing an object's radiance at each of several altitudes, a plot of radiance vs altitude can be generated as shown in Figure 2.B-8. The value of $L_i(0,0)$ can be found by extrapolating from the plot of Figure 2.B-8 to zero altitude. By repeating this procedure for objects of differing radiance, it is possible to establish a data set consisting of radiance observed at the sensor altitude L(h,0) and radiance at the surface L(0,0). Linear regression of $L_i(0,0)$ on $L_i(h,0)$ yields a slope equal to the atmospheric transmission over the bandpass sensed and an intercept equal to the path radiance $L_u(h,0)$. The radiance from the surface for any view angle can then be computed since

17

D=f(POSITION)

FILM IMAGE

DENSITY

LOG EXPOSURE

D

FILM
PROCESSOR

E

FILM WRITER

EXPOSURE

VOLTS

V

SENSOR

VOLTS

V_{BB}

RADIANCE

L_{BB}

L

BLACKBODY
REFERENCE
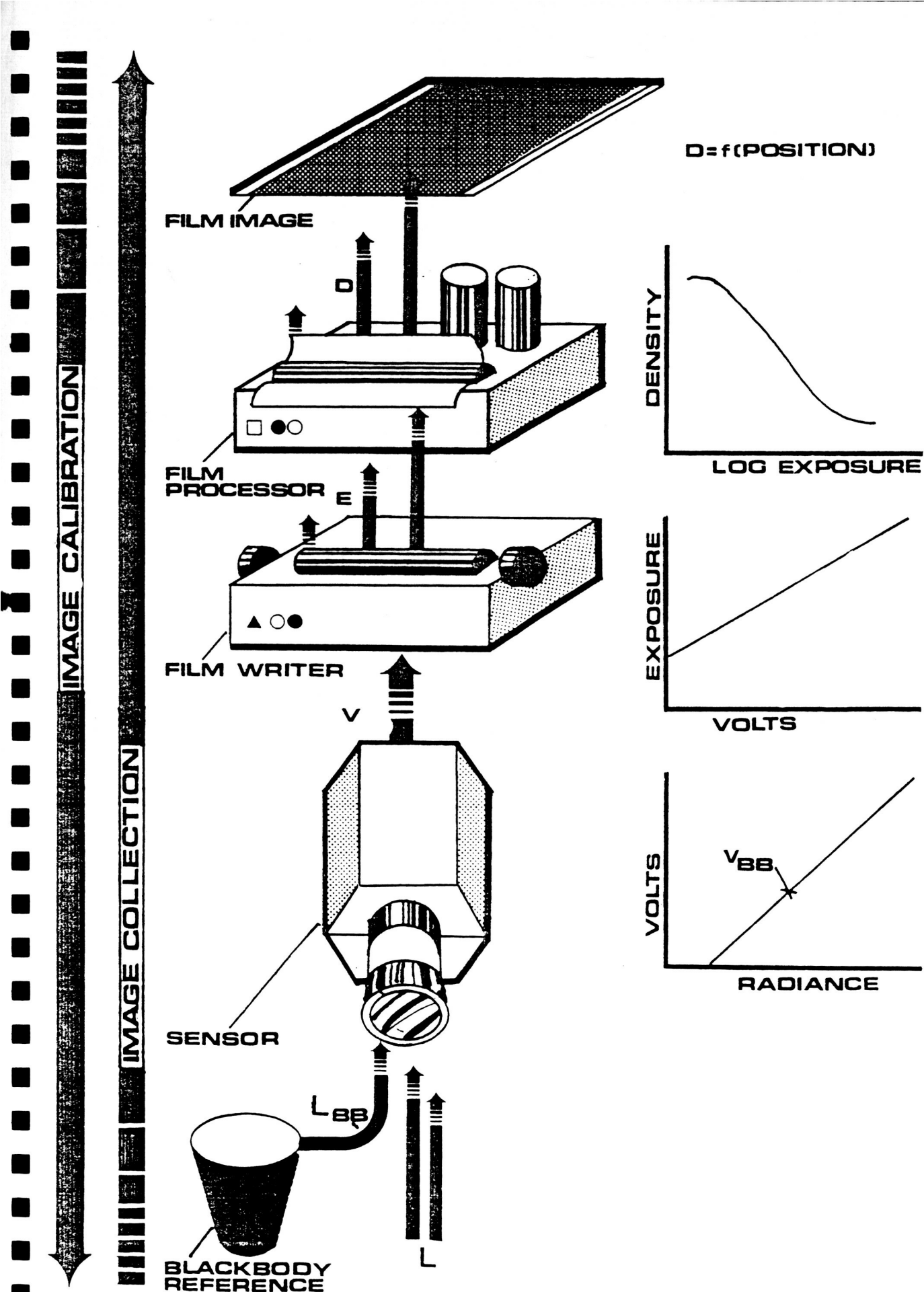
2.B-7   Calibration of Imagery for Quantitative Data Extraction

3000

Altitude [Feet]

60   Radiance [watts m^{-2} sr]   40

0
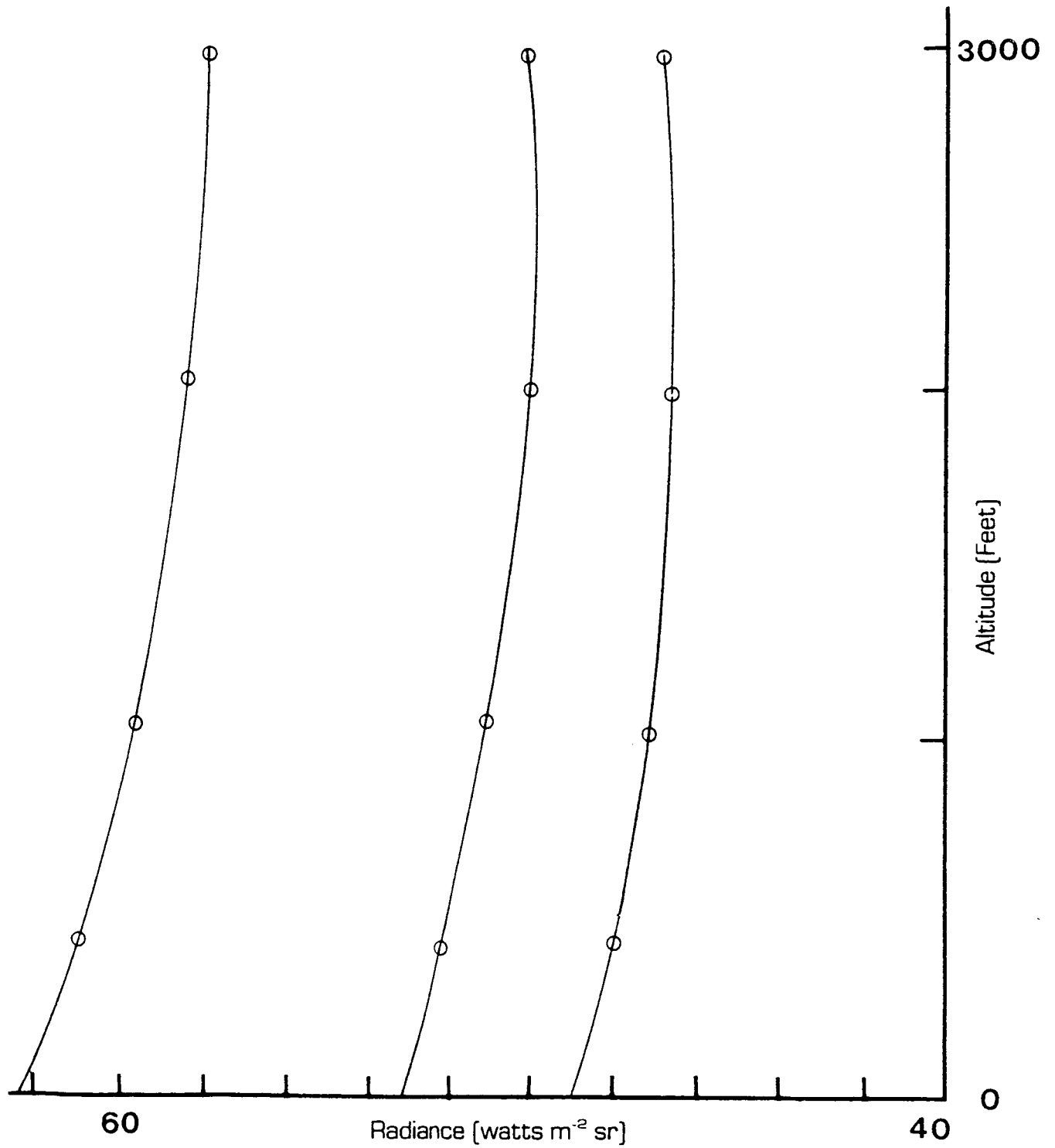
Radiance vs. Altitude

2.B-8   Sample Plot of Radiance versus Altitude for Different
         Targets

$$\tau(h,\theta) \cong \tau(h,0)^{sec} \qquad\qquad (2.B\text{-}10)$$

and

$$L_u(h,\theta) \cong \tau(h,0)^{sec\,\theta-1} L_u(h,0)sec\,\theta * \qquad (2.B\text{-}11)$$

It is also possible to compute the value of L_D if an object such as water, whose angular emissivity is known, is viewed at two angles. If this same object is viewed at two distinct angles, then equation 2.B-3 can be solved by substitution of L_T leaving L_D as the only unknown.

Schott (1979) has demonstrated that this profile technique is quite workable for removing atmospheric effects in the 8-14 µm spectral region. In particular, blindfold tests conducted over several days yielded standard errors of $0.4^\circ C$ when predicted temperatures were compared with observed kinetic temperature values. Because of this demonstrated accuracy, Schott's multiple altitude technique for computing atmospheric transmission and path radiance will be used as the standard for evaluating the values obtained by LOWTRAN and for generating large area water temperature values or predicted radiances.

2.C Experimental Design

The primary thrust of the experiment involved near simultaneous ground truth and satellite data collection. On two occasions, once for TM4 and once for TM5, water temepratures from grab samples were available from the Canada Center for Inland Waters. However, the major source of ground truth data were intended to be from LWIR scanner data obtained from simultaneous underflights (c.f. Figure 2.C-1). These data were to be acquired over regions of the Laurentian great lakes where large areas of uniform temperature could be expected and where large thermal differences would occur. Water was designated the ideal target because of its high thermal inertia. Figure 2.C-2 shows a TM6 full scene image of Lake Ontario when the spring thermal bar is well developed. This is an ideal target because of the large thermal

---

*approximation valid for large τ, i.e. for atmospheric windows and short path lengths.

DIRECTION OF ORBIT

L_U

L_U

τ

L_D

L_D
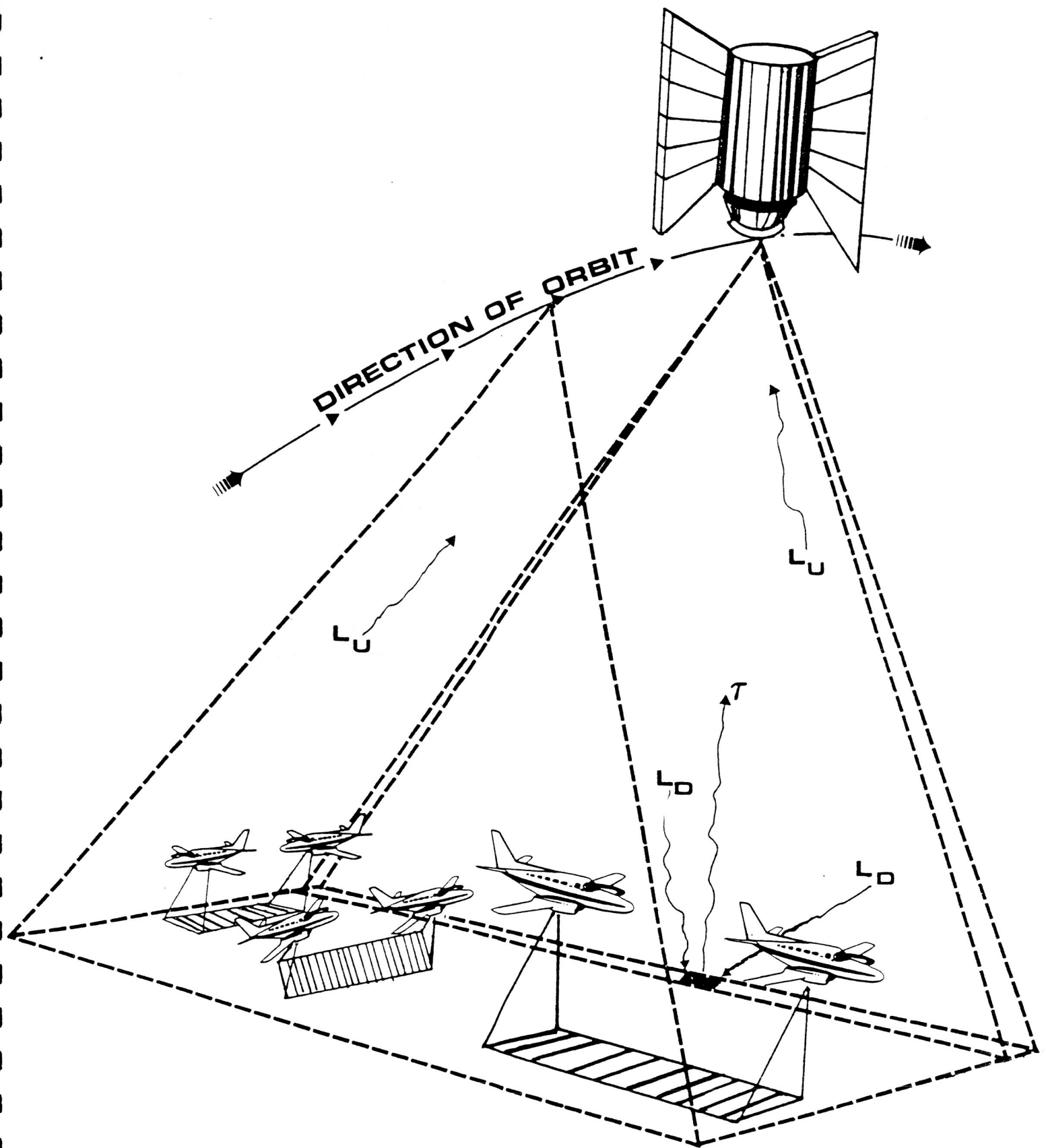
2.C-1   Calibration of Satellite Imagery using Underflights

2.C-2   TM Band 6 Full Scene Image Showing the Thermal Bar in
        Lake Ontario

differences and large regions of water at constant temperature. Realizing that the thermal bar only lasts several weeks, subtle thermal differences and the land water interface region were also accepted as target areas. The underflights were scheduled at the same time as the satellite overpass with flight lines at a series of altitudes perpendicular to the southern shoreline of Lake Ontario. Figure 2.C-3 illustrates the coverage region of a typical underflight. Also obtained at the time of the underflight were atmospheric data from the nearest airport where radiosondes were released, as well as local surface temperature, dew point and barometric pressure.

The surface truth data and underflight data were to be combined to generate the full ground temperature set. These values were to be directly compared to temperatures generated by analysis of the observed satellite radiance and atmospheric propagation models. This would evaluate how well the satellite system could predict surface temperatures. In addition, the surface temperatures could be used to predict radiance at the spacecraft using the propagation models and theoretical approach discussed in Section 2.B. These radiances could be compared with satellite observed radiance to evaluate spacecraft performance.

In addition, the ability to compute atmospheric propagation parameters such as transmission and upwelled radiance was to be tested. By flying the aerial LWIR system at a series of altitudes, the path radiance and transmission could be computed after the method of Schott 1979. (c.f. Appendix A) Analysis of LOWTRAN data indicated that the effective atmospheric depth was of the order of 6-8 kilometers. It should, therefore, be possible to measure the atmosphere's impact nearly to this limit and compare the modeled values with empirical values as illustrated in Figure 2.C-4. This would permit an assessment of the errors associated with the LOWTRAN propagation code. This is required to attempt to isolate errors in surface temperatures predicted by the satellite or radiances observed by the satellite.

The experiment was also designed to empirically measure atmospheric propagation parameters to the spacecraft in the TM band 6 spectral bandpass. This is accomplished by computing the TM band 6 in band surface radiance associated with surface temperature measured by the aircraft. If these are regressed against the surface radiance values observed by the TM band 6 sensor, the slope and intercept yield the atmospheric transmission and path

23

2.C-3   TM 6 Image showing Underflight Coverage Area

Legend:
— — — Atmospheric Propagation Model
— — — Underflight Observations
.... Extrapolated Data

Approximate Limits Of Data Collected (Underflight)

Altitude [km.]

10

8

6

4

2

0

1.0 .5 0
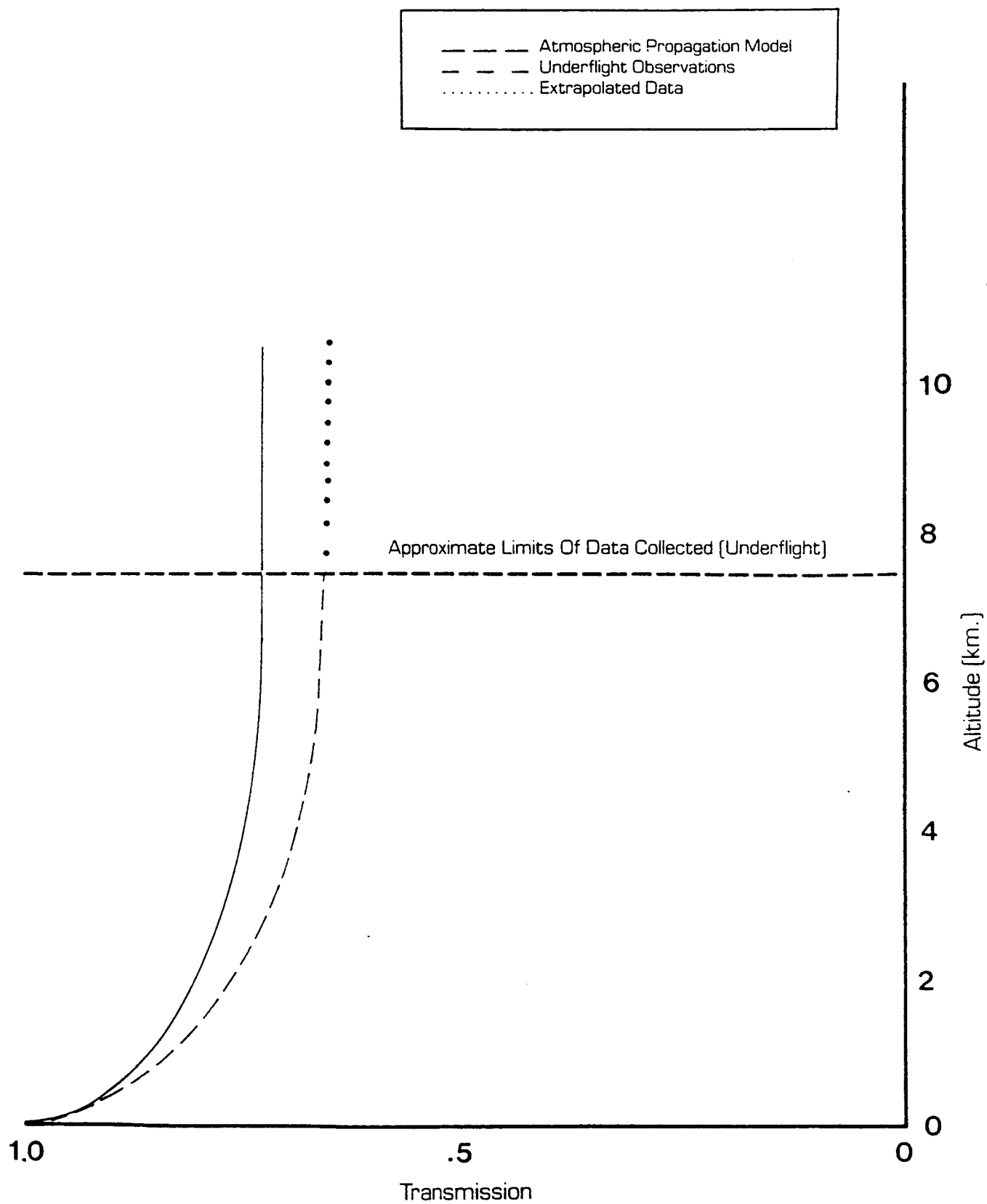
Transmission

2.C-4 Sample Plot of Atmospheric Transmission As a
        Function of Altitude

25

radiance respectively according to equation 2.B-9 (N.B. this assumes the TM band 6 calibration is correct). These empirically derived values can also be compared to the values obtained in the TM band 6 passband using the LOWTRAN propagation model.

The next section describes the collection and analysis effort that resulted from this experimental design.

2.D Data Collection and Analysis

This section describes the instrumentation and procedures used in acquiring and processing the satellite, aircraft, radiosonde and ground truth samples.

2.D.1 Data Collection

Table 2.D-1 contains a listing of the dates and types of data acquired on this effort. The radiosonde data were all acquired at Buffalo, NY and the surface meteorological data were acquired at Rochester, NY. The water surface temperature values were obtained by the CCIW as part of standard scheduled cruises on the great lakes. These data were obtained as grab samples at preselected locations over a several day period encompassing the satellite overpass.

The aerial LWIR data were acquired with RIT's infrared scanning system flown in a chartered Aztec C aircraft. The scanner has a 1 milliradion instantaneous field of view (IFOV), and a total field of view of 120°. It is operated with a thermally controlled blackbody and uses a point slope calibration method requiring regular calibration of the system gain. The systems 8-14 μm spectral response function is shown in Figure 2.D-1. Data were also collected using a narrower spectral filter matched to the satellite response function, but the reduced signal level precluded the use of these data. The system writes photographic imagery while collecting and employs a FM tape recording system for backup. Figure 2.D-2 shows a schematic of the data collection system. A sample image and the corresponding satellite subscene are shown in Figure 2.D-3.

Appendix B contains flight logs and pertinent data used in the analytical

26

Table 2.D-1 Data Collection Parameters

Date	Underflight Site TM Sensor	CCIW Data	Aircraft Data	Aircraft Altitude Range	Radiosonde Data	Local Meteorlogical Data
9/13/82		Yes	No		Buffalo, NY	Rochester, NY
9/22/84	Russel 5 Station	Yes	Yes	100-15,000 ft.	Buffalo, NY	Rochester, NY
10/6/84	Ginna 5 Station	No	Yes	500-20,000 ft.	Buffalo, NY	Rochester, NY
5/24/85	Russel 5 Station	No	Yes	500-15,0000 ft.	Buffalo, NY	Rochester, NY

effort.

2.D.2 Satellite Data Analysis

The satellite data analysis consisted of identifying scene coordinates corresponding to ground truth data, observing the digital count at that location and converting the digital count to radiance within the bandpass. All processing was done using CCT P tapes.

The scene coordinates were identified from latitude and longitude information corresponding to each ground truth sample obtained from the CCIW. Coordinate transforms were generated using well defined features on the reflected channel images and assuming geometric registration between channels. The validity of this assumption is documented by Malaret et al. 1985. The location of image coordinates for the underflight points was done using a 512 x 512 pixel, image subscene, incorporating the region imaged in the underflight. By visual analysis of the aerial LWIR image and the TM band 6 image corresponding points were identified.

Once the points of interest were identified, digital count values were obtained. These values were then converted to mean radiance within the bandpass using the header calibration data supplied by NASA, i.e.

$$L = L_\lambda(\lambda_2 - \lambda_1) = DC\ (R_{max} - R_{min})/255 + R_{min}\ (\lambda_2 - \lambda_1) \qquad (2.D-1)$$

where L is the blackbody equivalent radiance within the bandpass incorporating sensor response characteristics $[mWcm^{-2}sr^{-1}]$.

L_λ is the mean spectral radiance over the bandpass of interest incorporating the sensor response function $[mWcm^{-2}sr^{-1}\mu m^{-1}]$.

R_{max} and R_{min} are the maximum and minimum scene spectral radiance values read from the CCT header $[mWcm^{-2}sr^{-1}\mu m^{-1}]$ (i.e. they are the fundamental calibration constants as described by Barker et al. 1985).

λ_1 and λ_2 are the wavelength limits of the passband as defined by Markham and Barker 1985 $[\mu m]$.
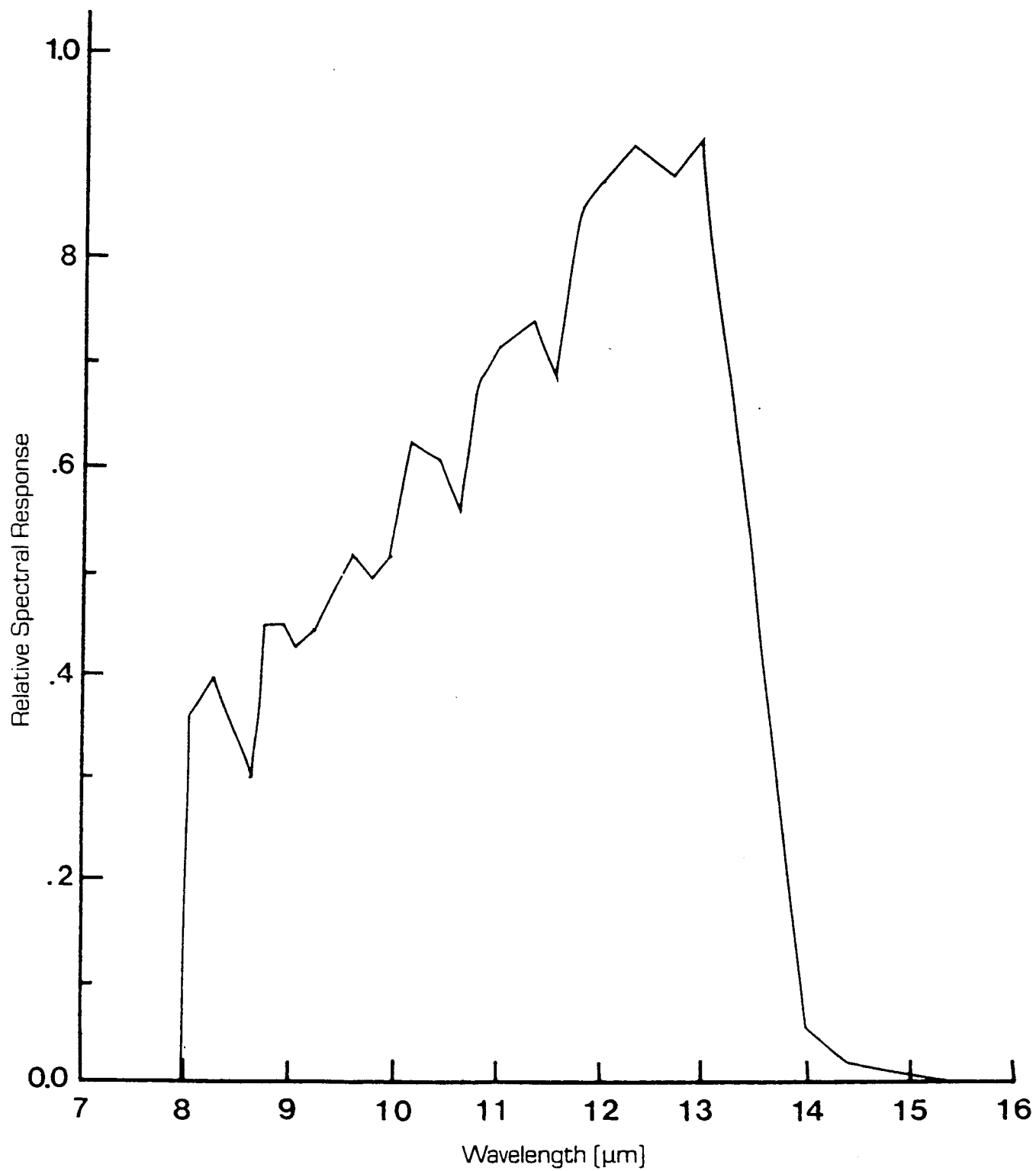
2.D-1   Spectral Response of IR Scanner System

2.D-2   Infrared Scanner Configuration

DEWAR

DETECTOR

MIRROR

FILTER WHEEL

TELESCOPE

BLACK BODY CONTROL

BLACK BODY REF.

GYRO

SCANNING MIRROR

ROLL COMP.

ELEC.

SYNC

SYNC CHOPPER

TAPE

ROTATING MIRROR

FILM PLANE

TARGET

SCAN DRIVE MOTOR

GMT

A.
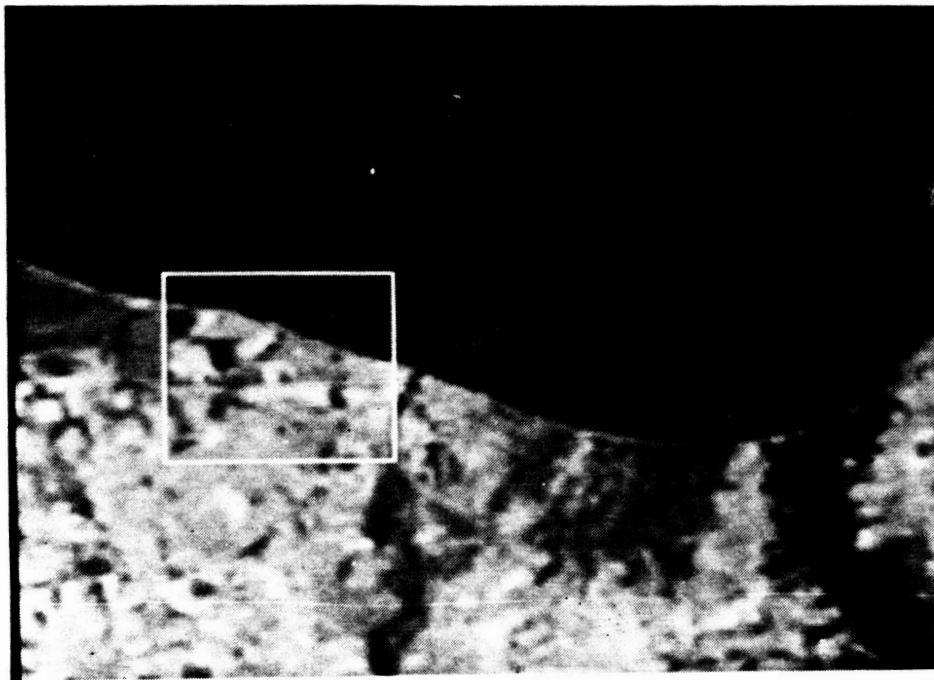
B.

2.D-3   Thermal Infrared Images a. Aerial Line Scan Image of Lake
         Ontario Shoreline, b. TM Subscene of the Lake Ontario
         Shoreline [N.B. the aerial image has considerable geometric
         distortion]

The radiance values at the sensor can be converted to apparent temperature by reverse solution of the Planck radiation equation. This was accomplished on this study by piecewise linear interpolation of a lookup table consisting of radiance and temperature values in 1K steps. The radiance values were generated by a Simpson's rule solution of the Planck equation. This conversion could also employ the method suggested by Lansing and Barker 1985 for TM4 Band 6 where:

$$T = K_2/[Ln(K_1/L - 1)] \qquad (2.D-2)$$

where;

L = spectral radiance $mWcm^{-2}sr^{-1}\mu m^{-1}$

$K_1 = 67.162[mWcm^{-2}sr^{-1}\mu m^{-1}]$ and $K_2 = 1284.3K$ for TM4

$K_1 = 60.776[mWcm^{-2}sr^{-1}\mu m^{-1}]$ and $K_2 = 1260.56K$ for TM5 (NASA 1984)

This approach, while not used here, is in good agreement with the more exact approach used over the approximately 20K range in temperature observed in this study.

The radiance and apparent temperature values analyzed by this method could then be used in comparison with underflight and surface radiance values using the methods described earlier. In particular equation 2.B-9 could be solved for the surface radiance associated with each point by utilizing the transmission and path radiance values obtained from the atmospheric propagation model.

2.D.3 Surface Truth Data Analysis

Figure 2.D-4 shows an example of the CCIW sampling station's used for the 13 Sept. 1982 Landsat 4 overpass. The surface grab sample data must be treated with considerable caution. Under the best of circumstances, it represents a point reading which must be correlated with the reading from the TM band 6 sensor which integrates over a 14,400 m^2 area. In addition, the grab samples are usually an integration of the first few centimeters to tens of centimeters of water temperature. Finally, for the data available here, the sample times may have been up to 48 hours different than the satellite sample time. All of these factors must be considered when these or any other point sampling data are utilized. In general, we would expect the surface

32

2.D-4   TM Band 6 Image Showing the Location of CCIW Sample Points

data to exhibit greater dynamic range than the temperature predicted by the satellite. This is because the local area thermal extremes sensed by the grab samples will be integrated with more moderate temperature regions by the large footprint of the Band 6 sensor.

Given these considerations, we felt that surface truth data should only be used with caution.

2.D-4 Aerial LWIR Image Analysis

Analysis of the LWIR aerial imagery involves conversion of recorded film density to observed radiance or apparent temperature and then use of the theoretical approach discussed earlier.

Photographic densities were read using either macro or micro densitometers available at RIT. All density readings were corrected to double diffuse density values to account for slight differences in optical density for different devices. (These differences result from different optical geometries in the measurement device.) Figure 2.B-7 illustrates the process of converting density to apparent radiance. The film density is the result of film exposure and photographic processing effects. The film exposure is varied by applying a voltage to the glow modulator tube used in writing the film. In flight, a set of known voltages are applied to the glow modulator tube and density steps recorded. These steps are used to generate a density-voltage curve which combines the top two curves in Figure 2.B-7. The density voltage curve is interpolated in a piecewise linear fashion to compute voltage levels. The voltage to radiance relationship is linear for any fixed gain setting. The form of the relationship is established separately for each set of scanner settings used in flight. The relationship can be expressed as:

$$L = g \ V + b \tag{2.D-3}$$

where;

L is the radiance reaching the sensor $[wcm^{-2}sr^{-1}]$

g is the sensor gain L/V established during preflight calibration for each gain setting.

b is the radiance intercept controlled by the DC restore level of the sensor which is referenced to the blackbody.

34

Thus, knowing the blackbody setting corresponding to a known radiance and the gain setting, equation 2.D-3 can be solved by the point slope method. This calibration is quite precise because the blackbody is introduced into the optical train ahead of the first optical element so that all near field radiation by the optics is included in the calibration process. Using the density to voltage step table generated in flight, and the voltage to radiance relationship derived from gain and blackbody setting, any scene density or the corresponding signal level recorded on magnetic tape can be converted to the radiance reaching the sensor.

During data collection, the scanner images a set of objects at several altitudes ranging from flight altitude to near ground level (150m). As indicated in the theoretical discussion, the radiance for each of the objects used in this set is plotted against altitude and extrapolated to ground level for use in the computation of atmospheric transmittance and upwelled radiance. As seen in Figure 2.D-5, the shape of the curve used to extrapolate to ground radiance is not always obvious and varies considerably with radiance level. In order to define an appropriate curve shape, the modified LOWTRAN model described earlier and detailed in Schott 1983 was exercised to compute radiance as a function of altitude for several surface radiance values. The curves illustrated in Figure 2.D-6 were then slid along the radiance or apparent temperature axis and evaluated for goodness of fit with each data set. The best fitting curve for each object was located using least squares methods and used to extrapolate to the expected surface radiance. In this way the phenomenological form of the LOWTRAN model could be used without relying on its absolute fidelity. We feel that this is a significant improvement in the profile method over the visual or straight line extrapolations previously used.

Using this profile approach, transmission and path radiance values were computed for each altitude of interest. Downwelled radiance was computed from modeled parameters as described in Section 2.B.2. These values were then used to compute surface radiance or apparent surface temperature values for comparison with the satellite derived data.

35
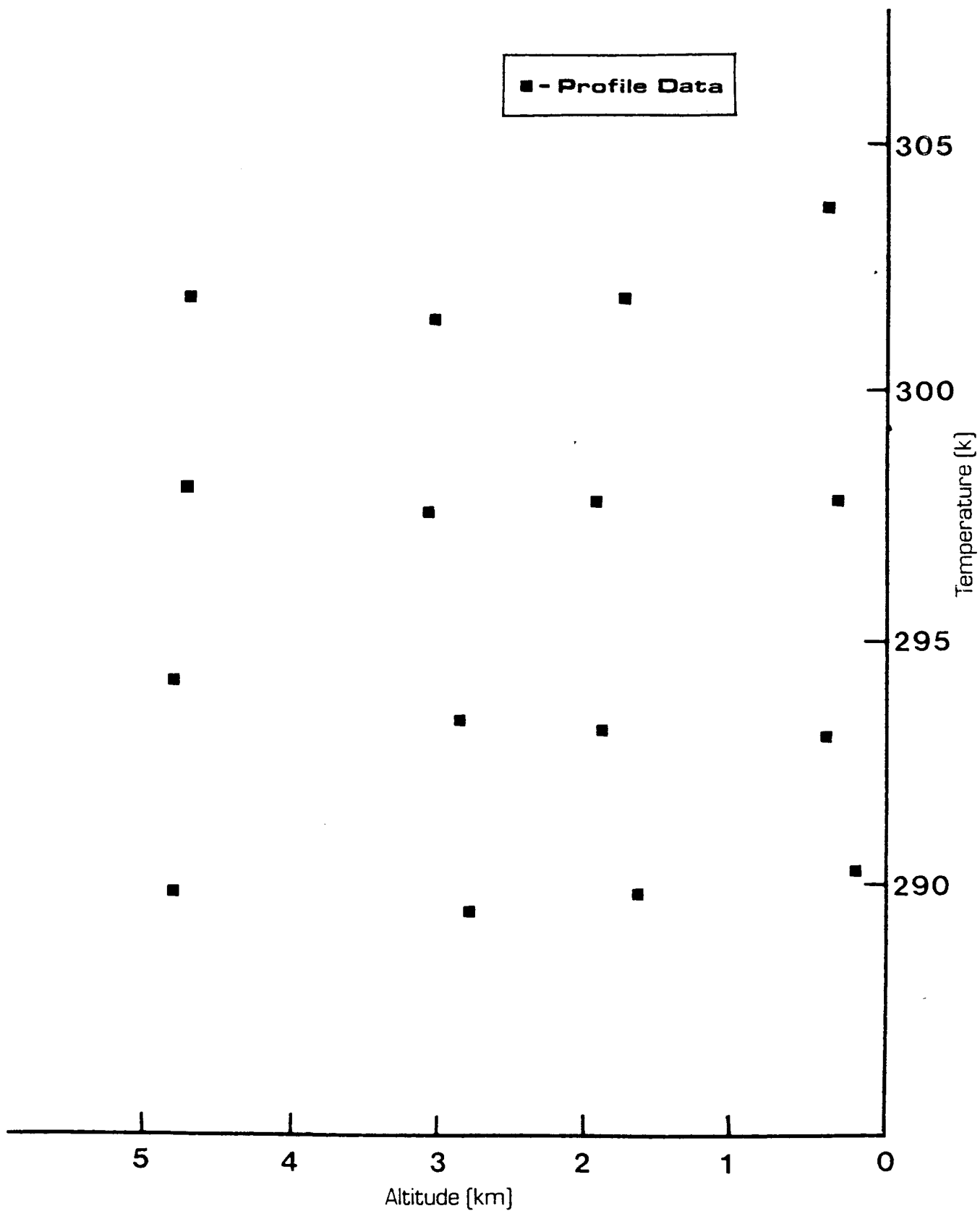
2.D-5 Sample Plot of a Profile Data Set
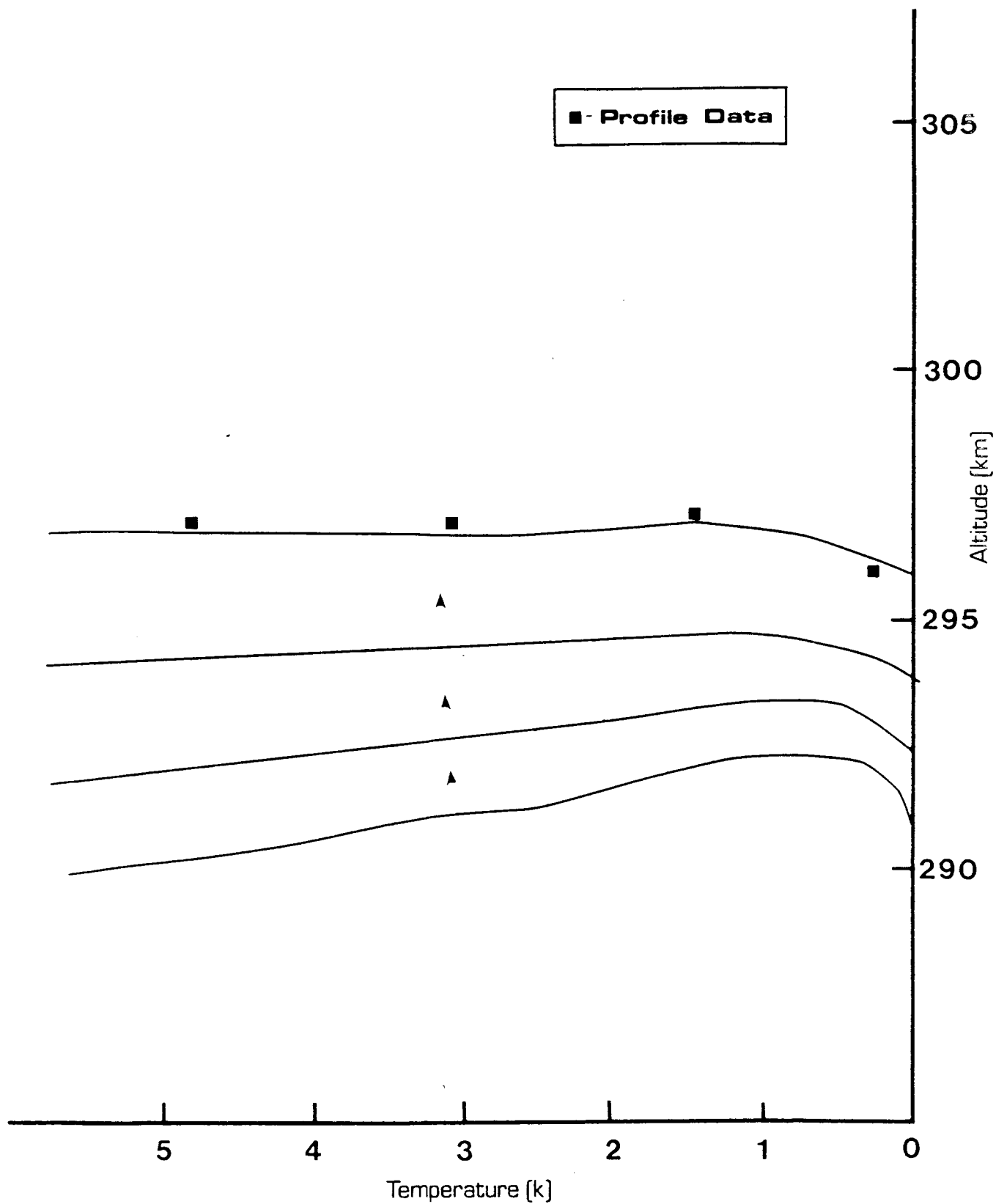
2.D-6   Illustration of Fitting Modeled Curves to Profile Data Set

2.D.5 Application of the LOWTRAN Model

The LOWTRAN 5A model is described in more detail in Section 2.B. The model used here was modified to incorporate the spectral response of the sensor and the scattering correction suggested by Ben-Shalom et al. 1980. The importance of this correction is illustrated in Figure 2.D-7 for the input data listed in Table 2.D-2.

This figure illustrates that without this correction the upwelled radiance at very high altitudes continuously decays in an unrealistic fashion for this passband. This would cause the overall radiance to decay in an identical fashion since the transmission term, and therefore the source radiance term, are essentially constants above 7 to 15 Km.

For each data set analyzed, the 7 a.m. radiosonde data at Buffalo, NY were used to characterize the atmosphere approximately 2 1/2 hours later sixty miles east near Rochester, NY. In order to account for this difference, the surface air temperature, dew point temperature, etc. at Rochester are used to adjust the radiosonde values as illustrated in Figure 2.D-8. The importance of this correction is illustrated in Figure 2.D-9 where the expected apparent temperature as a function of altitude are shown for the corrected and uncorrected cases. The apparent temperatures observed by the aerial line scanner are also shown. It is clear from this example that very careful attention must be paid to properly characterizing the atmosphere if radiation propagation models are to be used with any accuracy.

It is important to recognize that the mean integrated transmission computed by the basic LOWTRAN code cannot in general be directly utilized. Rather the effective radiance reaching the sensor, including spectral corrections for sensor response, must be computed for several values over the radiance range of interest. The surface radiance incorporating the sensor response is also computed for these same radiance values. The regression of expected radiance at the sensor versus surface radiance yields the effective transmission and path radiance as the slope and intercept respectively. This approach was utilized for all the studies reported here. In general, the effective values are only slightly different than the mean values because the atmospheric transmission, sensor response and blackbody spectral radiance are all reasonable well behaved functions of wavelength over the sensor passband

38
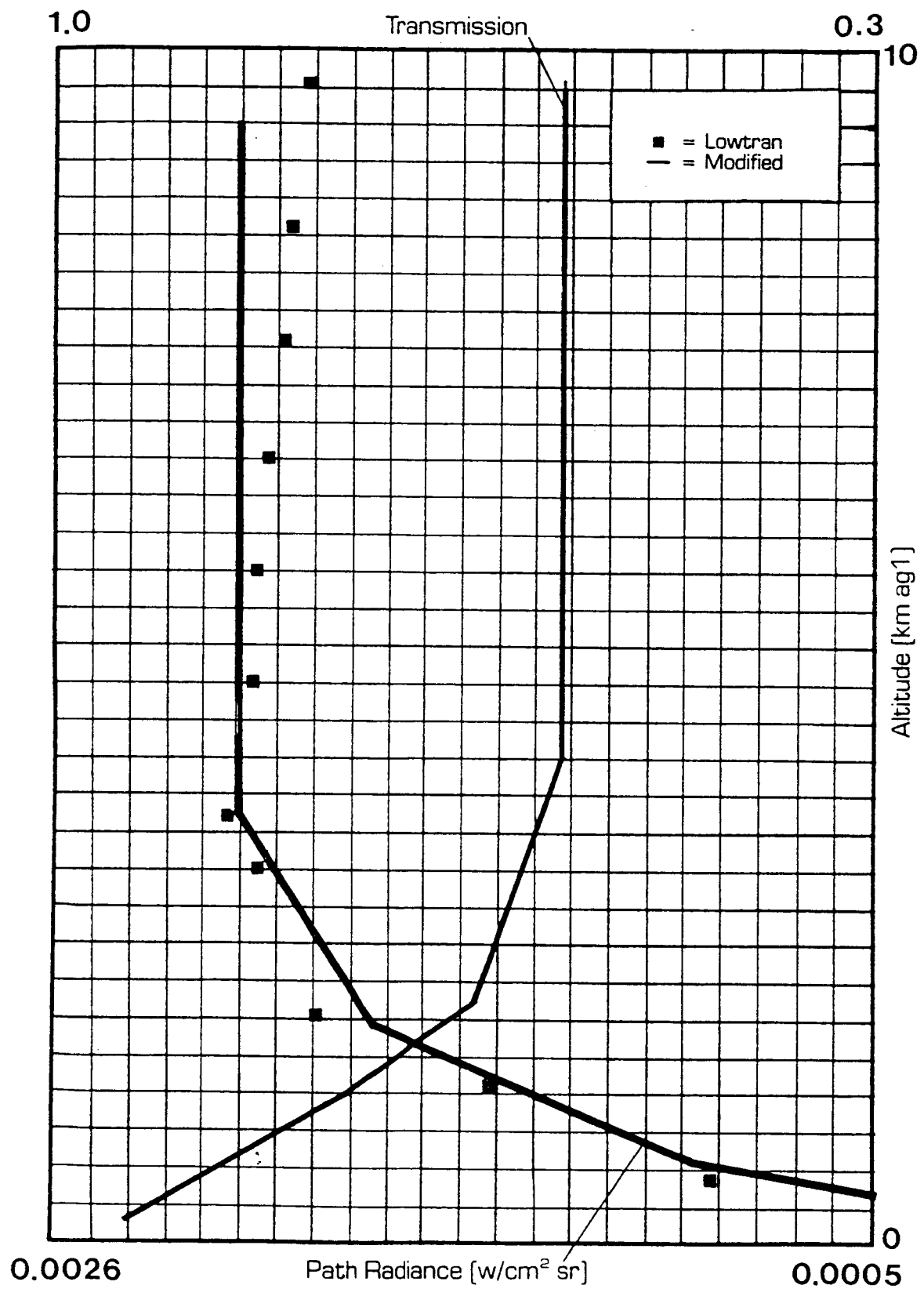
2.D-7 Sample Plot of Path Radiance and Transmission as a Function of Altitude

39

TABLE 2.D-2 - Input Data for LOWTRAN code

Radiosonde Input Data for 8/14/78 - 7 p.m. EDT Buffalo Airport

ALTITUDE (km)	PRESSURE (mb)	TEMPERATURE (^{o}C)	DEW POINT(^{o}C)
0.218	994.6	30.0	16.1
0.984	912.0	22.9	12.7
1.313	878.0	10.0	12.7
1.591	850.0	16.9	10.9
1.763	833.0	16.7	4.6
1.929	817.0	16.5	2.8
2.452	768.0	12.8	1.4
2.618	753.0	12.6	2.3
2.923	726.0	10.4	3.5
3.050	715.0	9.3	3.2
3.226	700.0	8.4	2.1
3.526	675.0	6.3	0.3
3.809	652.0	4.0	-0.8
3.885	646.0	3.9	-2.1
4.128	627.0	5.1	-11.7
4.299	614.0	3.5	-12.1
4.512	598.0	2.4	-27.6
5.794	509.0	-6.0	-36.0
5.934	500.0	-6.0	-36.0
6.188	484.0	-7.5	-37.5
6.350	474.0	-8.4	-38.4
7.645	400.0	-17.3	-47.3
9.296	319.0	-30.7	-60.7
9.590	306.0	-33.5	-36.0

A value of IHAZE = 1 was used corresponding to a Rural Aerosol model with 23km visibility.
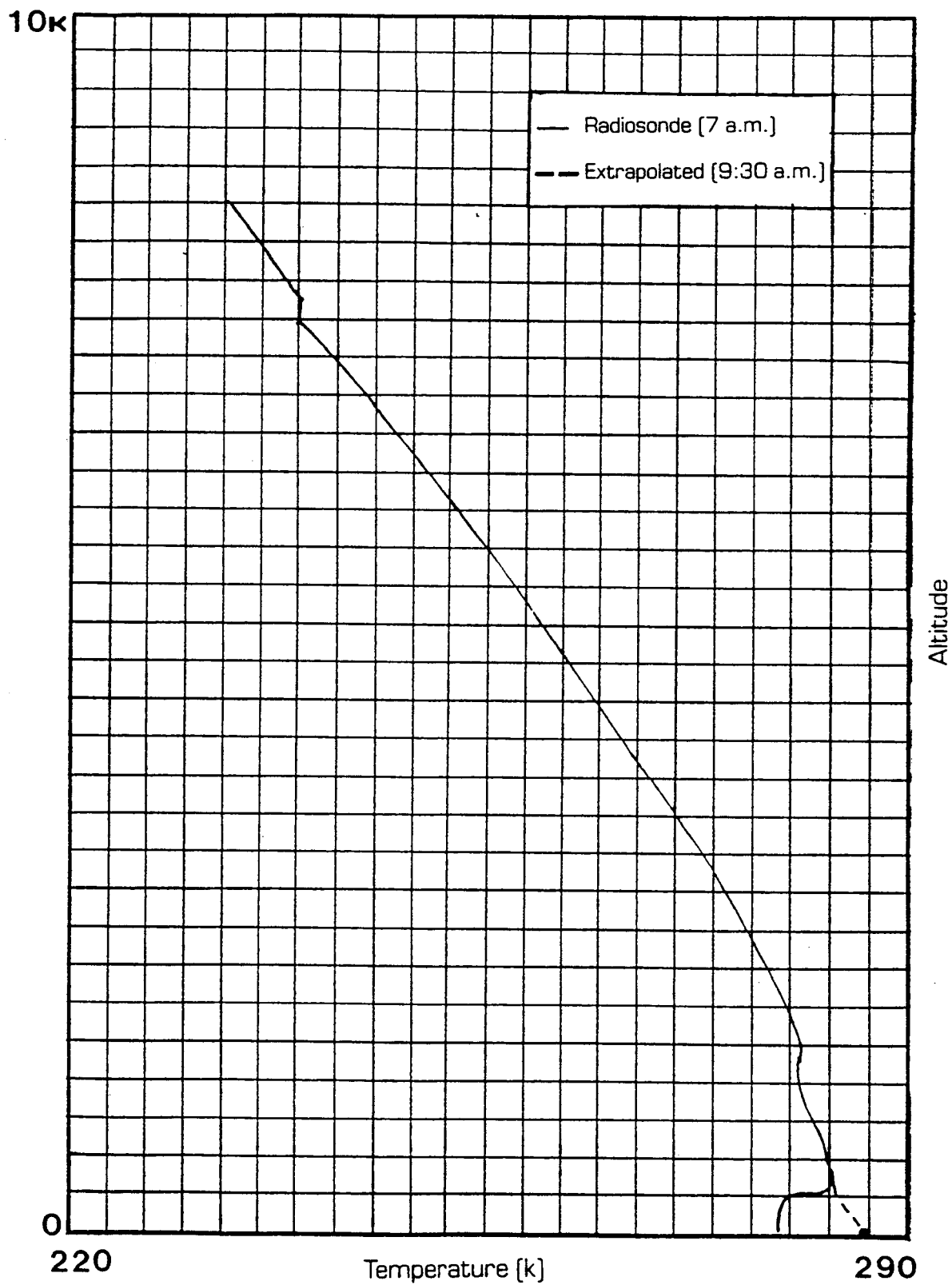
2.D-8   Sample Radiosonde Plot Showing Extrapolated Curve to
Match Observed Surface Temperatures
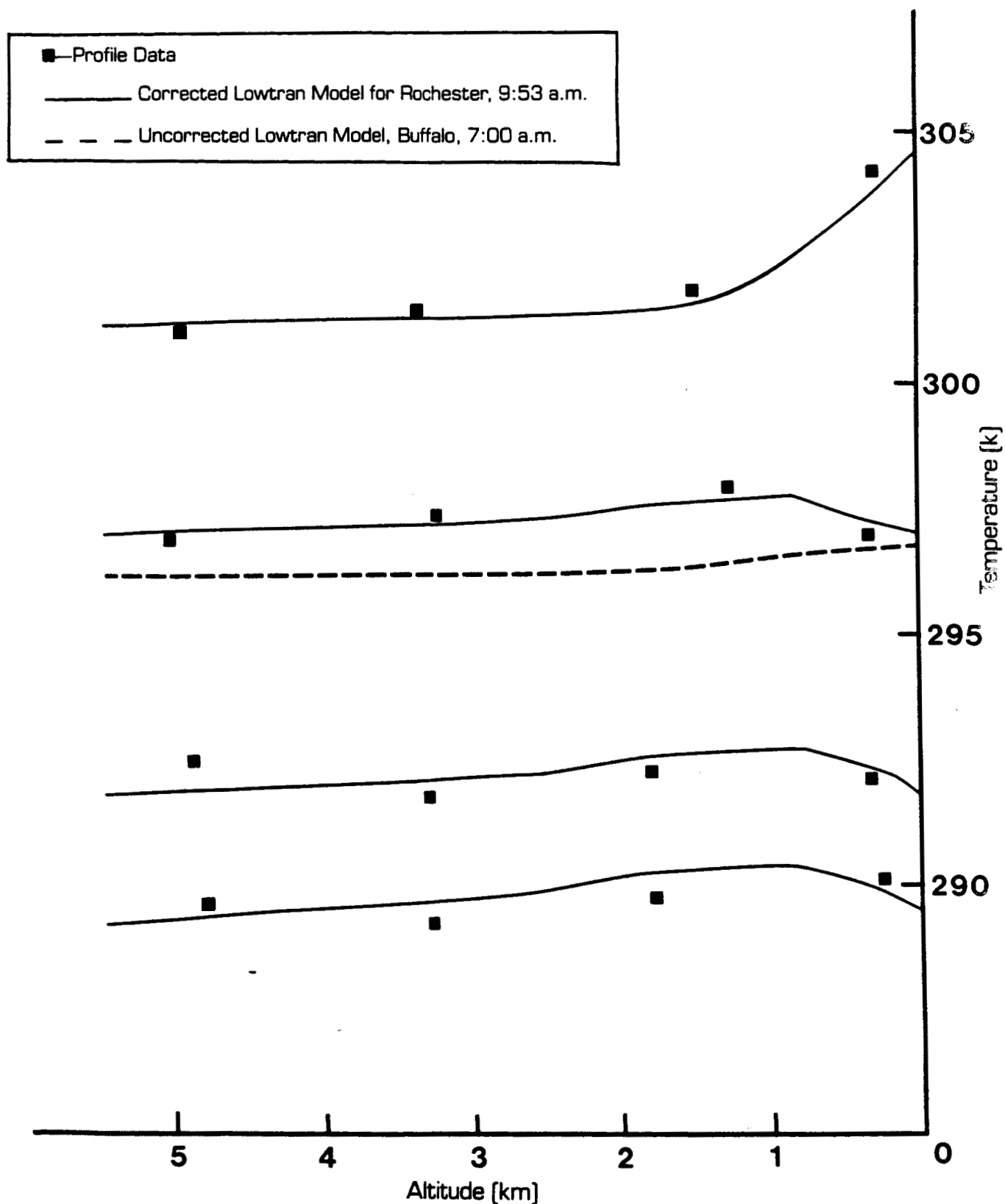
2.D-9 Profile and Modeled Values of Apparent Temperature versus Altitude Showing the Importance of Correctly Defining the Atmosphere

as illustrated in Figure 2.D-10.

The final effective atmospheric transmission and path radiance terms obtained in this fashion are then used to compute the radiance at the sensor, for a given radiance or apparent temperature at the ground. They are also used in reverse to predict surface radiance values from satellite observed radiance values. Finally, they were used for comparison with the empirically derived values obtained using the profile technique on the underflight data.
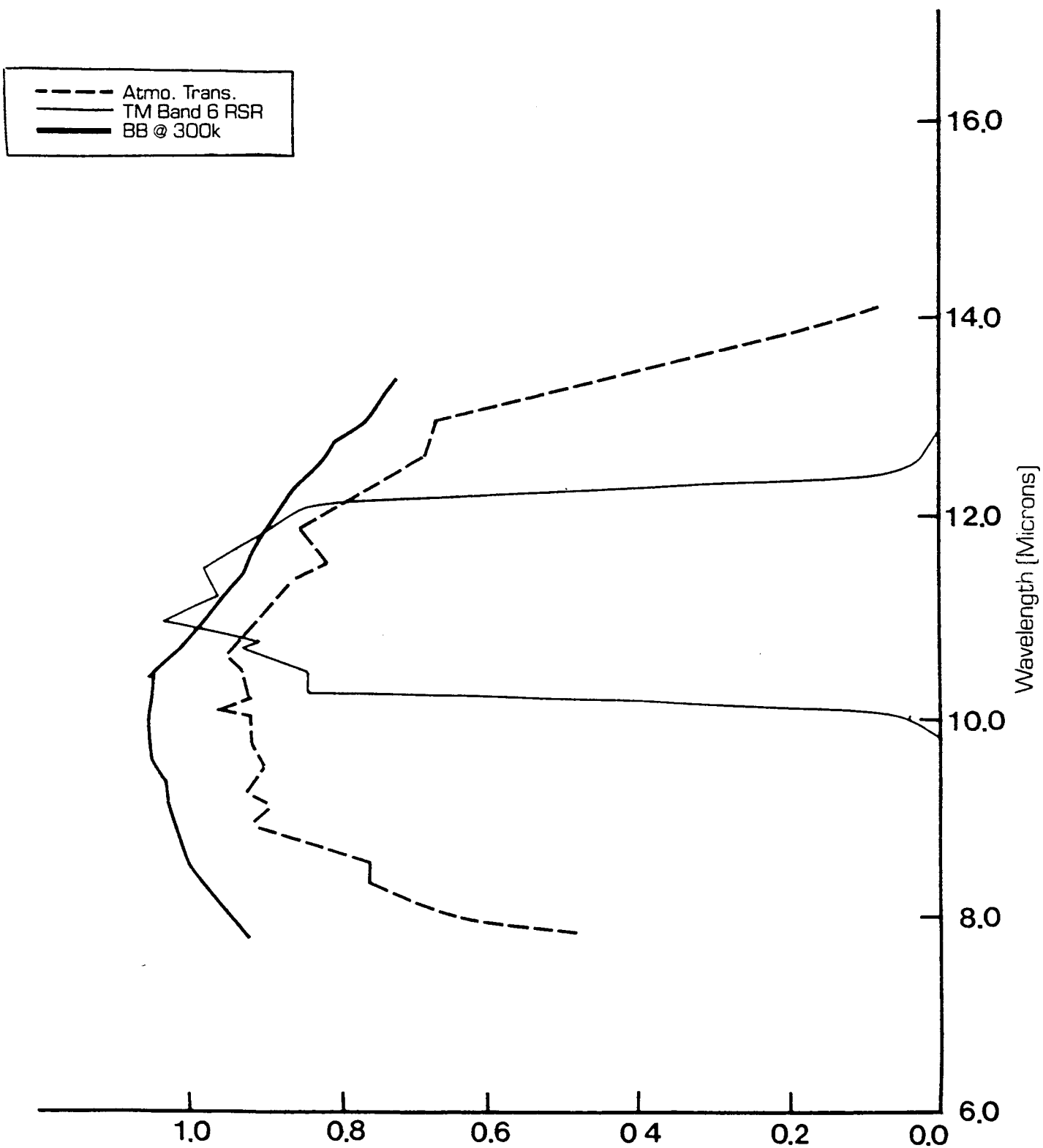
2. D-10 Spectral Radiance, Transmission and Responsivity for
Thematic Mapper Band 6

Legend:
- - - - - Atmo. Trans.
———— TM Band 6 RSR
▬▬▬ BB @ 300k

Wavelength [Microns]

SECTION III

Results

Drawing on the technical approach and analytical methods discussed in the previous sections, the radiometric quality of the TM band 6 data were evaluated. This section contains the result of that effort in terms of residual errors in temperatures on the ground and errors in the atmospheric propagation models. Methods of processing and display of the thermal data in conjunction with the reflected bands are also presented.

3.A Residual Errors

The Landsat TM band 6 data were processed to kinetic surface temperature or apparent radiometric surface temperature using the methods discussed in the previous sections. Kinetic temperatures were computed only for water targets where an emissivity of 0.986 was assumed for water. The resulting values are plotted in Figures 3.A-1 through 3.A-4 for the four dates studied. Figure 3.A-1 shows the only Landsat 4 data studied and contains only ground truth data from grab samples. These data are in very good agreement, however, they cover a rather small dynamic range. In addition, the satellite data tend to show a smaller dynamic range than the grab samples. This is consistent with what would be expected from the integrating effect of the relatively large satellite footprint.

The data from 6/22/84 plotted in Figure 3.A-2 show the underflight derived temperatures in good agreement with the satellite derived values. Again a discrepancy with the grab sample data is observed, although these data show a greater dynamic range in the satellite data than the surface data. Even with all the problems associated with grab samples, it is difficult to identify a potential source for this phenomena other than the time difference between sampling and satellite overpass. In general, we believe that the variety of errors associated with the available grab sample data make it unsuitable for accurate calibration. In light of this, the remaining analysis concentrated on the underflight surface temperatures. The 6/22/84 data show an RMS error between the satellite predicted values and the aerially derived temperatures of 2.82K over a range of approximately 25K for 20 points. The raw data for these computations on each date are contained in Appendix C. The data are in generally good agreement with only a few points at the high extreme of the

45
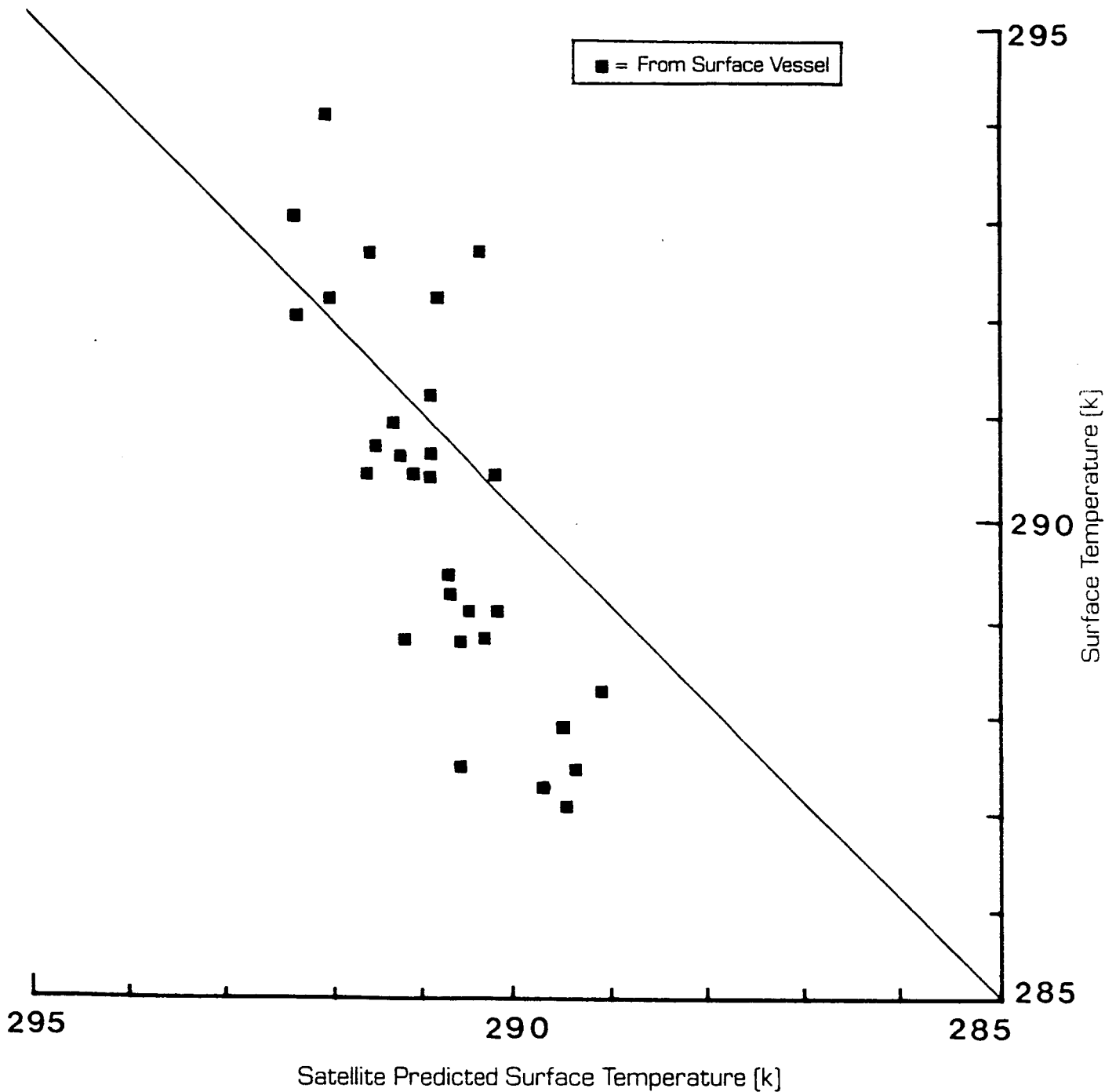
3.A-1   Plot of Satellite Derived and Surface Truth Temperatures for
        9/13/82 Data Set [TM4]
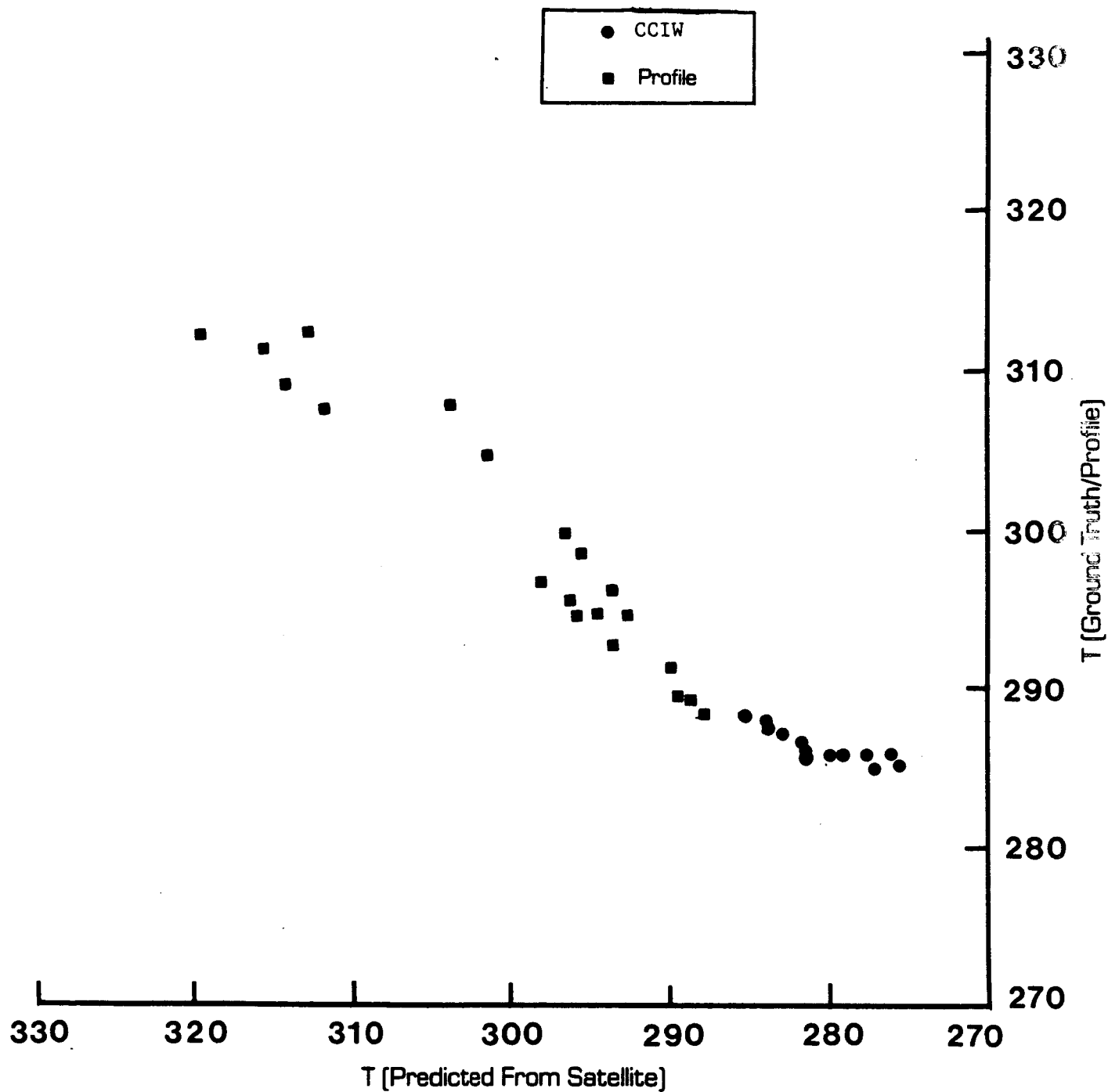
3.A-2   Plot of Satellite Derived and Data Set Surface Truth
        Temperatures for 6/22/84 Data Set (TM5)
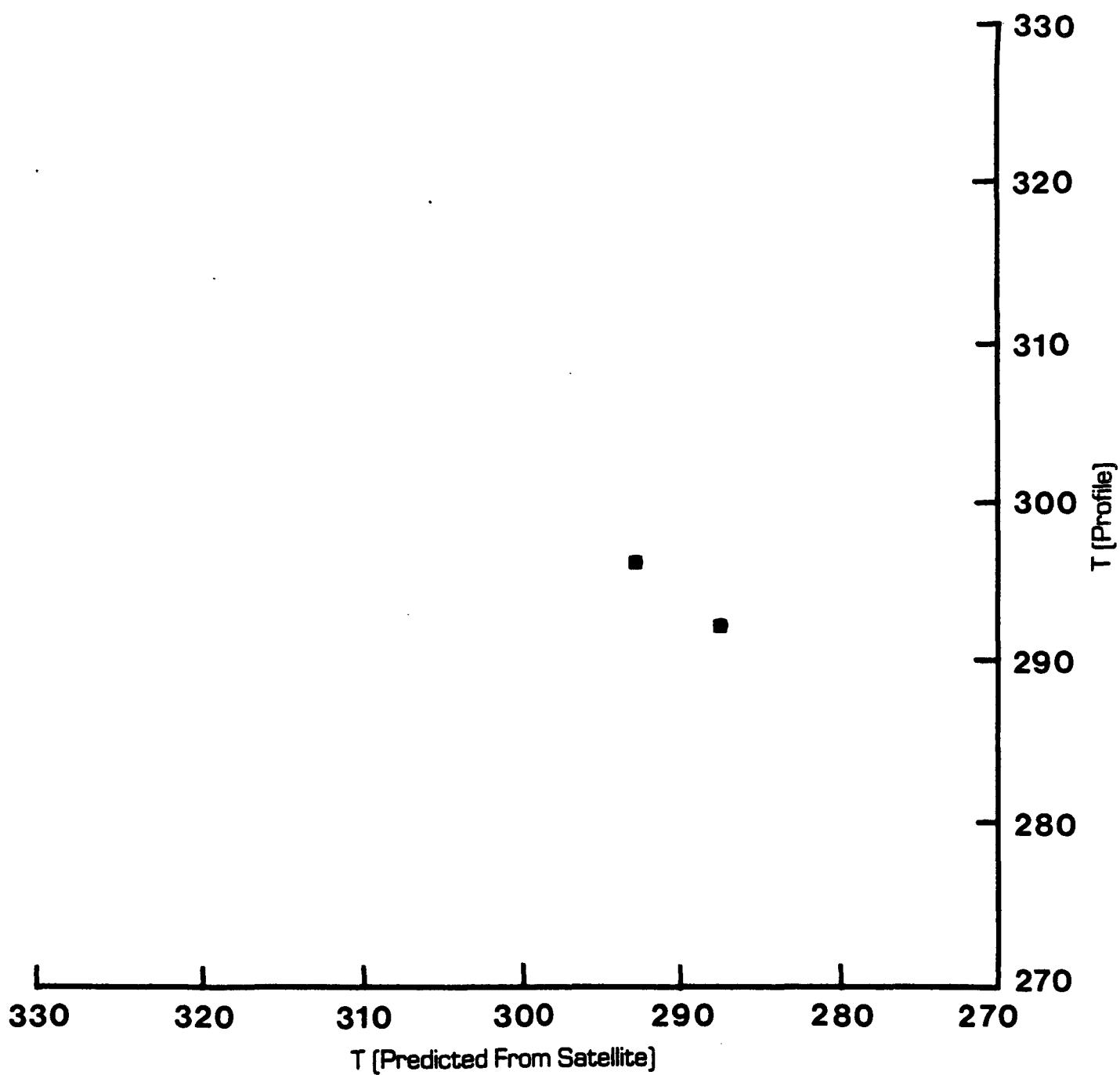
3.A-3 Plot of Satellite Derived and Surface Truth Temperatures for 10/6/84 Data Set (TM5)
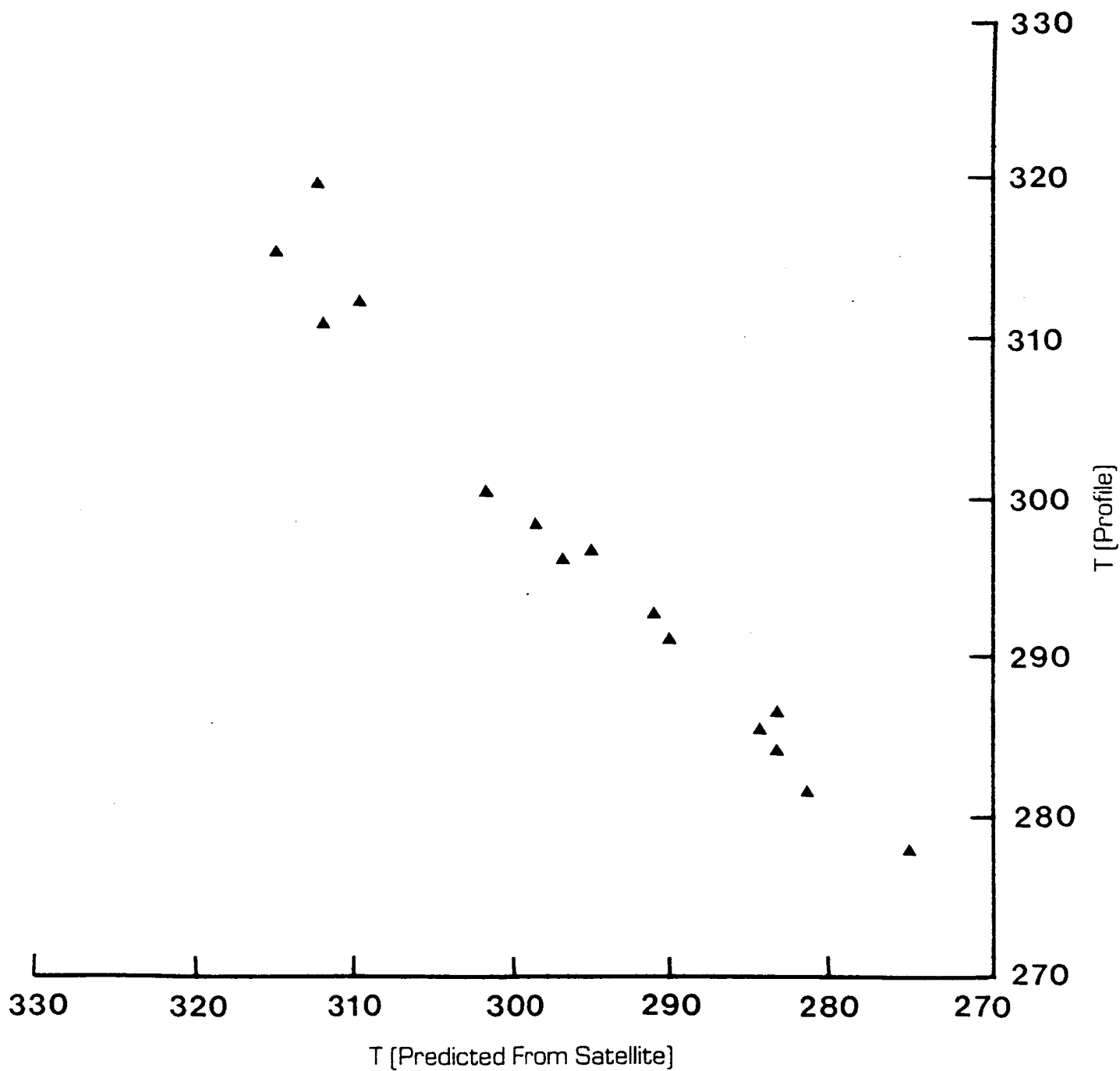
3.A-4   Plot of Satellite Derived and Surface Truth Temperatures for
         5/24/85 Data Set [TM5]

data set exhibiting significant errors. The average value of the differences between the two sets of predicted values is +0.97K indicating a bias in the data with the satellite predicted values slightly higher than aircraft derived values. In order to evaluate the relationship between the aerial and satellite predicted values, a linear regression analysis was performed on the data set. The slope, intercept and R^2 value for the data set were 1.101, -29 and 0.92 respectively. If for the moment one assumes no error in the aircraft data, then the interpretation of these parameters would proceed as follows. The slope greater than unity indicates that either the estimate of atmospheric transmission is slightly low or that the gain on the satellite was higher than it was believed to be. The bias toward high satellite predictions could result from underestimating the magnitude of the upwelled radiance or from a corresponding high bias in the satellite internal calibrator. We will discuss the likelyhood of these types of errors occurring in the next section.

Table 3.A-1 contains a listing of these same types of parameters for all the dates studied, including combinations of the dates for the Landsat 5 aircraft profile results. These combined data are plotted in Figure 3.A-5. Note that the 10/6/84 data are comprised of only two points. These data were generated from an aircraft flight the day prior to the satellite overpass and represent the measured apparent surface temperature for a large uniform region near shore and a second region well offshore. Because of the time difference between the two collections, these data were not considered heavily in subsequent analysis. However, because of the high thermal inertia of water and the large volumes involved, we would not expect significant changes in large area temperatures over short time spans and have not, therefore, completely rejected this data set

In reviewing Table 3.A-1, we note that the profile data sets exhibit the following general characteristics. The slope of the regression equations varies slightly about one with the combined results yielding a slope of one. This tends to indicate that the gain and atmospheric transmission errors are either properly accounted for or effectively offsetting each other. The bias errors for these same data sets indicate that the predicted satellite values are consistently slightly high. This indicates a slight bias in the internal calibrator or a tendency for the atmospheric propagation models to underestimate the upwelled radiance term. In the next section we will more thoroughly evaluate these possibilities based on an evaluation of the empirically measured and modeled

Table 3.A-1

Comparison of surface temperatures predicted by the satellite and measured by grab samples and aircraft analysis

Sensor	Dates	RMS Error(K)	Regression Results*				Reference Data	Range (K)	N	BIAS $T_{sat} - T_{ref}$
			Slope	Intercept(K)	R^2	Resid. Error (K)				
Landsat 4	9/13/82	1.48					CCIW	8	29	
Landsat 5	6/22/84	2.82	1.101	-29	0.92	2.53	Profile	23	20	0.97
Landsat 5	6/22/84	7.14	2.12	-327	0.81	1.23	CCIW	5	14	
Landsat 5	10/6/84	6.24					Profile	4	2	-6.0
Landsat 5	5/24/85	2.12	0.9503	15	0.98	1.93	Profile	37	13	0.61
Landsat 5	6/22/84 & 5/24/85	2.57	1.004	0	0.95	2.43	Profile	37	33	0.83
Landsat 5	6/22/84, 10/6/84 & 5/24/85	2.89	1.014	-4	0.93	2.86	Profile	37	35	0.44

*$T_{satellite}$ = Slope * $T_{aircraft}$ + Intercept where $T_{satellite}$ and $T_{aircraft}$ are the surface temperatures measured by the satellite and aircraft or grab samples respectively.
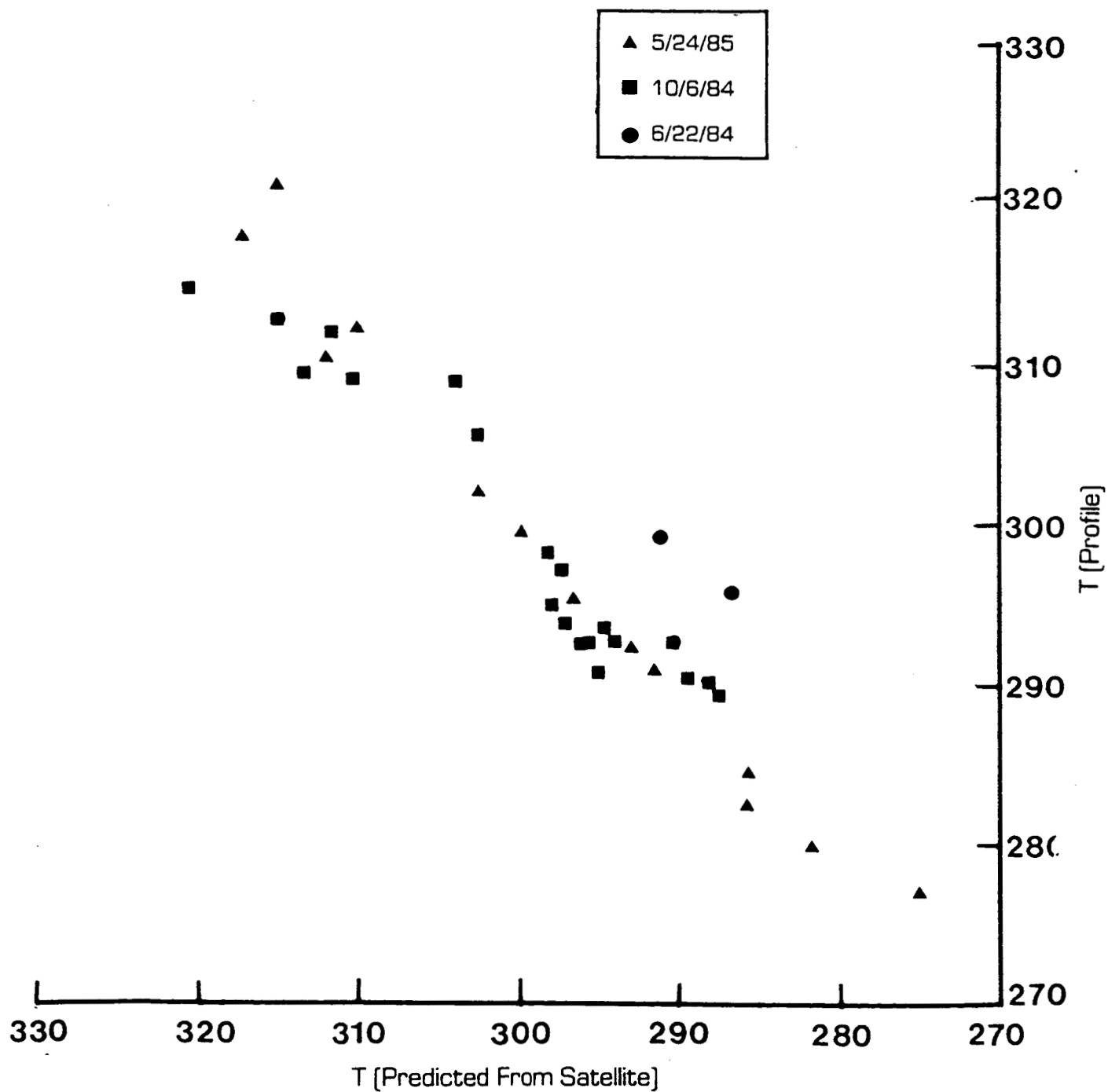
3.A-5   Plot of Satellite Derived and Surface Truth Temperatures for all Profile Data 6/22/84, 10/6/84 and 5/24/85 (TM)

atmospheric propagation parameters (τ and L_u).

3.B Evaluation of Atmospheric Propagation Models

In order to properly analyze TM band 6 data in terms of surface temperature, it is critical that we identify or develop a reliable atmospheric propagation model. The errors described in the previous section may be attributable either to satellite internal radiometric calibration or errors in the propagation model (again assuming for the moment no error in the temperatures predicted by the profile method). To assist in evaluation of this question, the modeled atmospheric parameters were empirically determined by the profile method. Recall that the sensor is operating over the 8-14 μm band and the atmosphere modeled is slightly different than for the satellite data. However, since the satellite window is included in the region measured by the aircraft, we believe the trends in the model should be similar over both windows.

Table 3.B-1 contains the results of this analysis for varying altitudes on selected dates. These data are obviously altitude and atmosphere dependent but tend to indicate that the LOWTRAN derived atmospheric transmission values are in general somewhat optimistic in this passband. Consistent with this the LOWTRAN derived path radiance values are slightly lower than the empirically derived values. This assumes that the profile derived values are correct. These data, while not in the specific passband of the thematic mapper, tend to indicate that the radiance range reaching the sensor should be slightly smaller than the LOWTRAN model predicts. These potential errors in the atmospheric propagation models would tend to explain the bias error discussed in the previous section. The corresponding transmission errors would have to be approximately offset by system gain errors to yield the results in Table 3.A-1. This concern is further reinforced by independent results observed by Lathrop and Lillesand, 1986. They indicate that the apparent temperature at the sensor is nearly identical with the surface temperatures collected in conjunction with the satellite overpass. These results linked with those of Malaret et al., 1985 and Wukelic et al., 1985, tend to support the concern that the system gain may be slightly higher than the internal calibrator indicates. Based on earlier results Schott and Volchok, 1985 had suggested that the sensor gain might be significantly in error. More thorough analysis of the underflight data, coupled with additional data sets, indicate that any gain errors are smaller than previously expected. Based on the nearly perfect slope value (i.e. slope of one) reported in Table 3.A-1 for the combined

Table 3.B-1

Comparison of profile and LOWTRAN derived transmission values

Date	Altitude	Transmission from LOWTRAN Incorporating Spectral Response	Transmission from Profile Technique	Ratio of LOWTRAN/Profile
6/22/84	15K	0.714	0.697	1.024
10/6/84	20K	0.814	0.673	1.210
10/6/84	15K	0.85	0.801	1.061
5/24/85	10K	0.765	0.630	1.214
6/25/83	0.33K*	0.805	0.876	1.033
6/25/83	0.66K*	0.859	0.813	1.057
6/25/83	1.33K*	0.801	0.762	1.051
6/25/83	2.0K*	0.772	0.746	1.035
Mean				1.086

*From Byrnes 1985

underflight data sets; the only source of gain error would be compensating error for the slightly over estimated atmospheric transmission expected from the LOWTRAN model.

3.C Overall Error Analysis

Because of the limited data base and the fact that the available data indicating errors in the atmospheric propagation model are for the 8-14 μm spectral window, it is difficult to specify a magnitude for the expected error in atmospheric transmission. Based on the empirical data utilized on this study alone, no correction for system gain would be warranted. However, the results reported by others and the potential errors in the atmospheric propagation models tends to indicate that if the models are over estimating atmospheric transmission by 8% then the system gain is high by approximately the same amount. The limited data base will not permit a more exact estimate and there is no reason at all to believe that these errors are exactly compensating. Therefore, based on the data collected as part of this effort, the best estimate would be obtained by correcting the satellite data as described here and assuming that the modified LOWTRAN code described above is nearly correct over the TM band 6 spectral bandpass. This conclusion is supported by the data reported in Appendix C where transmission was computed by regression of surface radiance derived from the profile temperature estimates with satellite radiances for the 6/22/84 and 5/24/85 data sets. The transmission differences between these two approaches are of the order of 8% but no consistent pattern is demonstrated.

In order to attribute an error to this approach, we consider the combined data set of Table 3.A-1 for the three dates on which good underflight data were available. For this data set the RMS error is only slightly greater than for the residual error for the regression analysis. Since the residual error in the regression analysis represents the error after a best case solution, it should represent a good estimate of the sampling error. This represents the combined errors due to random error in the estimation of temperature by the aerial and satellite technique and error in identifying the exact corresponding points in the two images. Since the error in the underflight measurements has been characterized at 0.4K and the sensor random error is approximately 0.5 due largely to quantization noise, the sampling misregistration error can be expressed as

$$\sigma_{samp} = (\sigma_{resid}^2 - \sigma_{gt}^2 - \sigma_{sat}^2)^{1/2} \qquad \text{(3.C-1)}$$

where; σ_{samp} is the error due to misregistration of aerial and satellite data.

σ_{resid} is the residual error from the regression analysis (2.86K for the combined data set.

σ_{gt} is the error in the ground truth data (0.5K).

σ_{sat} is the estimated random error in the satellite data (0.4K).

This yields an error due to sampling of 2.79K. This means that nearly all the error is due to location of common points.

If we then look at the RMS error, it can be expressed as

$$\sigma_{RMS} = (\sigma_{samp} + \sigma_{cal}^2)^{1/2} \qquad \text{(3.C-2)}$$

or

$$\sigma_{cal} = (\sigma_{RMS}^2 - \sigma_{samp}^2)^{1/2} \qquad \text{(3.C-3)}$$

where; σ_{cal} is the error in the radiometric calibration and atmospheric propagation models. For the combined profile data of Table 3.A-1 it takes on a value of 0.75K. The combined system error can be expressed as

$$\sigma_{sys} = (\sigma_{cal}^2 + \sigma_{sat}^2)^{1/2} \qquad \text{(3.C-4)}$$

σ_{sys} is the expected error in temperature associated with the combined sensor and calibration procedure errors. Its value based on the combined profile data set is 0.90K for one standard deviation. This can be interpreted to mean that if the procedures described here are used to predict temperature, 95% of the points should fall within 1.80K of the predicted value assuming no registration error and ramdomly distributed errors. This value should be reproducible if very large uniform surfaces were observed and if the aircraft sample site was well defined in the satellite image. This would be the case for images of the thermal bar such as seen in Figure 2.C-2. In this study only one underflight was available from this period, requiring the use of less desirable points for comparison.

3.D Multi-Resolution Data Fusion: Application to image analysis

The discussion to this point has concentrated on analysis of data with the same emissivity. Measurement of earth surface temperatures of diverse scene requires a method for dealing with varying emissivities. The governing equations and calibration approaches discussed in the previous section will readily permit temperature measurement if the emissivity is known. For a given material type an emissivity value can be assigned from a lookup table (N.B. much work remains to be done on the emissivity of natural surfaces). The limiting factor in this approach is associating a material type with each radiance value in a TM band 6 image. This limit is overcome by using the registered reflective channels of the TM to generate a land cover classification. This can either use a simple segmentation approach or a sophisticated discriminant analysis depending on the user's needs. Once classified, an emissivity can be assigned to each material class. These emissivities can then be used in the computation of surface temperatures. This process is detailed in Appendix D. Essentially the radiance values are acquired from the TM 6 data, the emissivities from the land cover data (from the reflective bands) and the atmospheric propagation data from the models described earlier. This means that the blackbody equivalent surface radiance or its associated temperature can be computed for each pixel at the resolution of the reflected channels. (This assumes the mean radiance sampled by the TM 6 band was equally made up from each subpixel corresponding to the reflective channels.) This results in a temperature or blackbody equivalent surface radiance map which appears to have higher resolution than the original LWIR imagery (c.f. Appendix D). This is visually more attractive. However, the quantitative accuracy for mixed thermal pixels is quite limited and only regions large enough to have uncontaminated thermal pixels should be treated quantitatively. The results of this approach are illustrated in Figures 2 through 5 in Appendix D.

57

SECTION IV

Conclusions and Recommendations

This study has demonstrated that consistent reliable surface temperature data can be obtained from the TM band 6 sensor using underflight calibration methods. It has further demonstrated that the expected error (1 std deviation) in surface temperature measurement using radiometric propagation models is of the order of 1.9K, assuming no emissivity error and no sample point location error. Finally a method of display of earth thermal features has been demonstrated that takes advantage of the registered shortwave images, the radiometric calibration procedures and the calibrated LWIR images.

There is some residual concern that the internal gain in the sensor may be slightly higher than the assigned value. However, the effect of this error on most scenes will be small as the results cited above indicate. We would, however, recommend a more detailed test involving calibrated radiometric underflights of the sensor with a sensor system spectrally matched to the satellite system. This would eliminate residual concerns of whether the error is in the propagation models or in the satellite sensor. We would also recommend ongoing research aimed at development of calibrated imagery. This would involve consideration of emissivity measurement of natural surfaces and methods of quantitatively merging multiresolution shortwave and longwave data sets.

Finally, an overall conclusion is that the radiometric quality and spatial resolution of the Landsat TM make it an extremely powerfull and useful tool for assessment of the temperature of earth surface features. However, the user must take care to recognize the various corrections necessary in quantitative analysis of LWIR imagery. In particular, spectral bandpass and atmospheric propagation corrections must be well understood and properly applied to achieve acceptable temperature errors.

58

SECTION V

References

1. Barker, John L., Editor, 1985 "Landsat 4, Science Characterization Early Results," Volume II Thematic Mapper, NASA Conference Publication 2355.

2. Barker, J.L., R.B. Abrams, D.L. Ball and K.C. Leung, 1985 "Radiometric Calibration and Processing for Reflective Bands on Landsat-4 Protoflight Thematic Mapper," Landsat for Science Characterization Early Results, NASA Conference Publication 2355.

3. Ben-Shalom, A., et al., 1980, "Sky Radiance at Wavelengths between 7 and 14 μm: Measurement Calculation and Comparison with LOWTRAN-4 Predictions," Applied Optics, Vol. 19, No. 6, pp. 838-839.

4. Bohse, J.R., M. Bewtra, and W.L. Barnes, 1979, "Heat Capacity Mapping Radiometer (HCMR) Data Processing Algorithm, Calibration, and Flight Performance Evaluation," NASA Technical Memorandum 80258.

5. Byrnes, Arthur E. and J.R. Schott, 1986, "Correction of Thermal Imagery for Atmospheric Effects Using Aircraft Measurement and Atmospheric Modelling Techniques," Prepared for Applied Optics, Vol. 25, No. 15.

6. Irons, James R. 1985 "An overview of Landsat-4 and the Thematic mapper," Volume II, Landsat-4 Science Characterization Early Results, NASA Conference Publication 2355.

7. Lathrop, R.G. and T.M. Lillisand, 1986, "Calibration of Thematic Mapper Thermal Data for Water Surface Temperature Mapping: Case Study on the Great Lakes (86-82)," (Personal Communication of results to appear in Remote Sensing of Environment).

8. Lansing, J.C. and J.L. Barker, 1985, "Thermal Band Characterization of the Landsat 4 Thematic Mapper," Proceedings of the Landsat-4 Science Characterization Early Results Symposium, NASA Conference Publication 2355.

References (continued)

9. Malaret, E., L.A. Bartolucci, D.F. Lozano, P.E. Anuta and C.D. McGillem, 1985, "Landsat and Landsat-5 Thematic Mapper Data Quality Analysis," Photogrammetric Engineering and Remote Sensing, Vol. 51, No. 9, September 1985, pp. 1407-1416.

10. Markham, B.L., and J.L. Barker, 1985, "Spectral Characterization of the Landsat Thematic Mapper Sensor," Proceedings of the Landsat-4 Science Characterization Early Results Symposium, NASA Conference Publication 2355.

11. Markham, B.L. and J.L Barker, Editors, 1985, "Special LIDQA Issue," Photogrammetric Engineering and Remote Sensing, Vol. LI #9, September 1985.

12. Schott, J.R., 1979, "Temperature Measurement of Cooling Water Discharged from Power Plants," Photogrammetric Engineering and Remote Sensing, Vol. 45, NO6.

13. Schott, J.R. and E.W. Schimminger, 1981, "Data Use Investigations for Applications Explorer Mission A (HCMM)," CAL #6175-M-1, NASA Accession #E81-10079.

14. Schott, J.R., 1983, "Target and Background Infrared Calculations for Tactical Space-Based Sensor Applications," RIT Report #PSI 82/83-51-3, Prepared for Naval Research Laboratories.

15. Schott, J.R. and J.D. Biegel, 1983, "Comparison of Modelled and Empirical Atmospheric Propagation Data," Presented at 27th SPIE Annual International Technical Symposium, San Diego, CA, August, 1983.

16. Schott, J.R. and W.J. Volchok, 1985, "Thematic Mapper Thermal Infrared Calibration," Photogrammetric Engineering and Remote Sensing, Vol. 51, #9.

17. Selby et al., 1978, "Atmospheric Transmittance," Radiance Computer Code LOWTRAN 4, AFGL-TR-78-0053.

18. Subbarayudu, J., 1979, "Heat Capacity Mapping Mission (HCMM) Validation Study," Systems and Applied Sciences Corporation Report #R-SAG-3/79-01 to NASA Goddard.

19. Wukelic, G.E., J.C. Barnard, G.M. Petrie and H.P. Foote, 1985, "Opportunities and Difficulties Associated with Using Landsat Thematic Mapper Data for Determining Surface Water Temperatures," ACSM-ASPRS Fall Convention 1985, Indianapolis, pp. 879-891.

20. 1980, Heat Capacity Mapping Mission (HCMM) Data Usery Handbook prepared by NASA Goddard.

A 79-38372

APPENDIX A

Excerpted From:

"Temperature Measurement of Cooling Water Discharged from Power Plants,"
Photogrammetric Engineering and Remote Sensing, Vol. 45, No. 6, June 1979, pp.
753-761.

JOHN R. SCHOTT
Calspan Corporation
Buffalo, NY 14225

Temperature Measurement of Cooling Water Discharged from Power Plants

A technique for calibrating a thermal infrared scanner was successfully tested.

INTRODUCTION AND SUMMARY

THE GROWING NUMBER and size of power facilities has stimulated the interest of scientists, legislators, and the public in the effects such stations have on aquatic environments. The impact of thermal dis-

cooling water discharged into a water body, the temperature value and spatial extent of the thermal plume are the parameters of interest. These thermal plumes can, in some instances, extend more than a mile from the discharge point and include temperature increases in excess of 15°F.

ABSTRACT: In an effort to resolve technical, operational, and cost problems associated with the existing approaches for measurement of water surface temperature, a program was initiated to develop and test a wholly airborne calibration of a thermal scanner system as an alternative. This technique involved development of a model relating the signal at the sensor to the surface temperature and the atmospheric effects contributing to the signal at the sensor.

Procedures were developed for collection and analysis of the thermal imagery such that the terms in this model could be calculated. Once these terms, including atmospheric transmission, sky radiation, and reflectance of the water, have been determined, the water surface temperature can be calculated. In an effort to evaluate this technique, a series of "blindfold" tests were made. In these tests, an airplane flew over a boat located at different positions in the water at different times and on different days. The aircraft values were then compared to the boat values, which had been withheld until the aerial determinations were made. Results of this test indicate that, on the average, the aerial measurements fell within 0.70°F of the boat temperatures (standard deviation ±0.59°F for 63 points). On the basis of these results, this wholly airborne approach, called the "angular calibration technique," is considered operational for airborne measurement of water surface temperatures.

charges on aquatic ecology and the effects on aquatic organisms that are drawn through cooling systems are of particular concern. In order to ensure proper protection and management of the environment as well as continued generation of required power, procedures must be developed to accurately assess environmental effects in a timely and cost-effective manner. In monitoring the

Airborne thermal infrared imaging systems have been used to study some of these problems.[1-3] These systems generate an image (similar to a photograph) of the heat energy radiated by water surfaces. For example, the brighter the water appears on the image, the higher the temperature of the water is. The advantage of this approach is that the thermal scanner can image the entire

surface area of a discharge plume in minutes. In this manner, all the internal detail as well as the shape and spatial extent can be easily determined. The disadvantage of this approach is that a boat is required to provide data needed to convert brightness levels on the image to temperature values.

In an effort to resolve technical, operational, and cost problems associated with the existing approaches, a program was initiated to develop and test wholly airborne calibration of a thermal scanner system so that precise thermal maps could be generated without requiring data from boats. This technique involved development of a model relating the signal at the sensor to the surface temperature and the atmospheric effects contributing to the signal at the sensor.

Procedures were developed for collection and analysis of the thermal imagery such that the terms in this model could be calculated. Data collection procedures included flying the aircraft at different altitudes over the same point in the water and flying parallel flight lines so that data from points in the water could be viewed at different look angles. These procedures add a minimal amount of time to data collection and provide sufficient data so that an analysis of the terms relating water temperature to the signal actually reaching the sensor can be calculated. Once these terms, including atmospheric transmission, sky radiation, and reflectance of the water, have been determined, the water surface temperature can be calculated.

In an effort to evaluate this technique, a series of "blindfold" tests was made.[4] In these tests an airplane flew over a boat located at different positions in the water at different times and on different days. The aircraft values were then compared to the boat values, which had been withheld until the aerial determinations were made.[5] Results of this test indicate that, on the average, the aerial measurements fell within 0.70°F of the boat temperatures (standard deviation ±0.59°F for 63 points). On the basis of these results, this wholly airborne approach, called the "angular calibration technique," is considered operational for airborne measurement of water surface temperatures.

This paper discusses the airborne calibration technique and the experimental test program. For the sake of brevity, the details of the airborne collection system are omitted and the assumption is made that the radiant energy reaching an airborne sensor can be converted to an apparent blackbody temperature equivalent.

THEORETICAL APPROACH

Thermal scanners generally detect radiation in the 8-14 μm bandpass. This section will discuss how the radiant energy detected by a sensor at aircraft altitudes (~600 m) is not only a function of temperature but is also functionally dependent on atmospheric and background terms. In addition, the types of measurements required to calculate the values of these additional terms will be defined.

All matter at temperatures above absolute zero radiates electromagnetic energy. The relation between blackbody radiant emittance, W, and temperature, T, in °K is expressed by the Stefan-Boltzmann equation

$$W = \sigma T^4, \tag{1}$$

where σ is the Stefan-Boltzman constant.

The general equation for a blackbody radiator is given by the Planck distribution equation,

$$W_\lambda = 2\pi c^2 h \lambda^{-5} (e^{hc/\lambda kT} - 1)^{-1}, \tag{2}$$

where W_λ is the radiant emittance per unit wavelength interval,

  c is the speed of light,
  h is Planck's constant,
  k is Boltzmann's constant,
  T is temperature, and
  λ is wavelength.

This equation, derived from quantum physics, is a function of the quantum radiation states within a blackbody cavity.

The Stefan-Boltzmann equation is obtained by integrating the Planck equation over all wavelengths.

The problem in using these equations is finding the dependence of W on temperature over a defined bandpass. The Stefan-Boltzmann equation indicates that radiant emittance integrated over all wavelengths varies as T^4, i.e.,

$$\int_0^\infty W_\lambda \, d\lambda = W = \sigma T^4. \tag{3}$$

To find the functional dependence on temperature in a finite bandpass, it is necessary to use a series expansion solution to the normalized integral of radiant emittance. This yields the fraction of energy less than a given wavelength, D, given by

$$D = \frac{\displaystyle\int_0^\lambda W_\lambda \, d\lambda}{\displaystyle\int_0^\infty W_\lambda \, d\lambda}. \tag{4}$$

64

These D values are tabulated in standard blackbody tables for ranges of T, λ, or λT combinations.[6] By finding the difference in D for two wavelengths, a relation can be developed between temperature and radiant emittance in a bandpass expressed as a fraction of the total radiant emittance.

If D is the fraction of the total energy emitted by a blackbody between the wavelength 0 and λ, then $D_1 - D_2$ is the fraction of emitted energy between λ_1 and λ_2. Since σT^4 is the total energy for a given temperature, then $W = (D_1 - D_2) \sigma T^4$ is the radiant energy emitted for a given bandpass. Values of W and T over the range of interest can be stored in data files on a computer. T can be calculated from the stored W values.

We can therefore express the radiant energy from a blackbody over the 8-14 μm bandpass ($W_{\Delta\lambda}$) as

$$W_{\Delta\lambda} = W_T = \int_{8}^{14} 2\pi c^2 h \lambda^{-5} (e^{hc/\lambda kT} - 1)^{-1} \, d\lambda.$$

(5)

This expression, however, is only true for a blackbody. A blackbody is a perfect radiator and absorber; therefore, all the incident energy is absorbed and reradiated. In practice, the bodies we will be concerned with will be gray bodies, which are not perfect absorbers or radiators in the 8-14 μm bandpass and thus have emissivities less than unity.

Emissivity (ϵ) is the ratio of energy radiated from a source to energy radiated from a blackbody at the same temperature. Thus, for a gray body,

$$W = \epsilon W_T.$$

(6)

In order to interpret the radiant energy reaching a point at any distance from the source, one must consider atmospheric or path effects; of prime concern is atmospheric transmission over the path lengths of interest. The atmospheric transmission window between 8 and 14 μm is the most useful for earth observation work for a number of reasons. It encompasses the radiant energy peak of 9.5 μm for objects near earth ambient temperature of 300°K. The transmission is quite high over the entire window, and the window is spectrally very broad, permitting integration over a sizable fraction of the total energy radiated.

Primary attenuation in the lower atmosphere is due to absorption by H_2O vapor, CO_2, and OH. These molecules absorb the radiation and reradiate it as a function of temperature, thereby introducing two noise terms into the system.

These terms can be included in the expression we have defined as follows:

$$W = \tau \epsilon W_T + W_A$$

(7)

where τ is the atmospheric transmission and W_A is the apparent radiant emittance from the air column between the source and sensor, as well as energy scattered into the sensor. It is important to keep in mind that W_A and τ vary as a function of atmospheric conditions on a given day and also within the air column because of layering effects in the atmosphere.

In addition to the radiant energy from the source itself, a certain amount of energy will be reflected from the ground. This energy comes from both the sun and the sky. Solar reflection effects can be avoided by proper orientation of flight lines. Skylight reflection effects can be expressed as $W_s \tau R$ and included in Equation 7, yielding

$$W = \tau \epsilon W_T + W_A + W_s \tau R$$

(8)

where W_s is the radiant energy from the sky incident on the surface observed, and can be associated with an equivalent sky temperature, T_s. R is the surface reflectance of the water.

Skylight irradiance comes from scattered solar radiation, radiation emitted from components of the atmosphere (especially the ozone layer and H_2O vapor), and energy from the Earth reflected by the atmosphere. All these effects combine to give the sky an apparent radiometric temperature as viewed from the ground. For our purposes, this is the blackbody temperature equivalent, T_s, associated with the amount of energy incident on the source over the bandpass of interest. T_s can vary considerably with sky conditions from about 300°K for heavy overcast to well below 250°K for clear sky conditions.

In evaluating the range of values for the reflectance terms, we recognize that reflection is dependent on look angle. In addition, we have mentioned that W_A and τ are dependent on the length and composition of the atmospheric path between the source and observation point. To recognize this dependence in Equation 8, the functional dependence on θ and h will be added to designate angular and height dependence, respectively,

where h is the height of sensor above terrain,

θ is look angle measured from the vertical, and

$$W(h, \theta) = \tau(h,\theta)\, \epsilon(\theta)\, W_T + W_A\,(h,\theta)$$
$$+ \tau(h,\theta)\, W_s\, R(\theta). \quad (9)$$

Limiting our discussion for the moment to vertical viewing, $(\theta = 0)$, results in

$$W(h) = \tau(h)\epsilon\, W_T + \tau(h)\, W_s\, R + W_A(h). \quad (10)$$

Letting $W(0)$ be the energy from the ground as it would be measured vertically at zero altitude, Equation 10 reduces to

$$W(h) = \tau(h)\, W(0) + W_A(h) \quad (11)$$

where
$$W(0) = \epsilon W_T + W_s R. \quad (12)$$

If $W(h)$ and $W(0)$ are known for a set of observed values, then, by least-squares analysis of Equation 11, $\tau(h)$ and $W_A(h)$ can be calculated. $W(h)$ and $W(0)$ represent the radiant energy observed by the sensor at flight altitude and ground level, respectively. In practice, the ground level measure is obtained by extrapolating a plot of altitude-versus-temperature to zero altitude using data collected over the same point at a series of altitudes, where radiant energy is converted to apparent blackbody temperature.

If we once again consider the angular viewing effects, Equation 11 becomes

$$W(h,\theta) = \tau(h,\theta)\, W(0,\theta) + W_A(h,\theta) \quad (13)$$

where

$$W(0,\theta) = \epsilon(\theta)\, W_T + W_s\, R(\theta), \quad (14)$$
$$\tau(h,\theta) = \tau(h,0) \exp (1/\cos \theta), \text{ and} \quad (15)$$
$$W_A (h,\theta) = W_A(h, 0)/\cos \theta. \quad (16)$$

These equations result from the increase in absorption with path length (Equation 15) and the increase in atmospheric radiation with path length (Equation 16). Since the path length increases as $1/\cos \theta$ for slant viewing and the effects on atmospheric emissions should be very nearly linear for small increases in path length through a given medium, Equation 16 is derived. Note that this assumption of linearity is only valid for increase due to slant viewing through a known atmosphere and is not necessarily valid for an overall increase in path length.

If observations were made at the same altitude of a given point through two different look angles, one of which may be taken as vertical for convenience, then Equations 10, 13, and 14 may be combined to yield

$$W(h, 0) = m\, W(h, \theta) - m\tau(h, \theta)\, W_s\, R(\theta)$$
$$- m W_A(h,\theta)$$
$$+ \tau(h, 0)\, W_s R(0) + W_A(h, 0) \quad (17)$$

where $m = \dfrac{\epsilon(0)\, \tau(h, 0)}{\epsilon(\theta)\tau(h,\theta)}$. $\quad (18)$

Recognizing this as a straight line in the form,

$$W(h, 0) = m W(h, \theta) + I \quad (19)$$

and solving for W_s in terms of m and I yields

$$W_s = \frac{I + m W_A(h,\theta) - W_A(h, 0)}{\tau(h, 0)\, R(0) - m\tau(h,\theta)\, R(\theta)}. \quad (20)$$

Least-squares analysis of Equation 19, with input data consisting of apparent temperatures (converted to radiant energy) measured along a line viewed vertically and then at a slant angle, will yield from Equation 20 a measure of apparent sky temperature as viewed from the ground.

We have assumed that the apparent temperature of the sky is a constant with respect to angle of observation. In general, this is not the case; rather, the zenith sky appears colder than the sky near the horizon because the atmosphere viewed vertically has fewer radiators. Because of the variability of sky conditions, a functional relationship between sky temperature and view angle is not readily defined nor are the errors introduced by the assumption of a constant sky easily evaluated. In order to minimize potential errors in measured sky temperature, the analysis discussed above can be conducted for a number of look angle combinations, and a simple relationship between T_s and θ can be developed.

Another solution would involve use of a vertical-viewing, upward-looking radiometer on board the aircraft. Measurement of vertical sky temperature at a number of altitudes and extrapolation to the apparent temperature of the nadir sky as viewed from the ground would eliminate one unknown in Equation 17. The equation could then be solved for the sky temperature at look angle θ (i.e., T_s associated with $R(0)$ would be known and T_s associated with $R(\theta)$ would be unknown).

Rewriting Equation 9 as
$$W_T = [W(h,\theta) - \tau(h,\theta)\, W_s\, R(\theta)$$
$$- W_A (h,\theta)]/\epsilon(\theta)\, \tau(h,\theta), \quad (21)$$

we find

$W(h,\theta)$ is a measured value;

$W_A(h,\theta)$ is obtained from Equation 16 and least-squares analysis of Equation 11;

$\tau(h,\theta)$ is obtained from Equation 15 and least-squares analysis of Equation 11;

66

W_s is obtained from Equation 20; and

$R(\theta)$ and $\epsilon(\theta)$ are tabulated values for water.

It should therefore be possible to measure the absolute value of surface waters based on the theories developed thus far. The next section contains procedural approaches for collection of necessary input data to solve for the values in Equation 21.

EXPERIMENTAL DESIGN

Our concern at this point is in defining procedures for collecting sufficient input data to permit the use of the theoretical procedures under discussion. Again, we will neglect, for simplicity, signal processing through the sensor and assume that apparent blackbody radiometric temperature can be measured at the sensor location by converting radiant energy to equivalent blackbody temperature.

As shown in Equation 11, the input data necessary to calculate the transmission term $\tau(h)$ and the additive target-independent energy from the atmosphere $W_A(h)$ consist of $T_B(h)$ and $T_B(0)$ corresponding to $W(h)$ and $W(0)$. $T_B(h)$ is simply the apparent blackbody temperature measured at altitude h with look angle $\theta = 0$. $T_B(0)$ is the apparent temperature measured at the surface of the water. This value cannot be measured directly but is obtained by a profile technique which involves a simple extrapolation process for data collected at a series of altitudes to a zero altitude case obtained by consecutive flights over the same target.[7] A target consists of an area of uniform temperature either large enough to be directly below the aircraft during the profile or within about $10°$ from the nadir and distinct enough to be identifiable on the profile images. At angles much larger than $10°$ the assumption of vertical viewing during the profile no longer holds.

The minimum data input required for Equation 11 is $T_B(h)$ and a corresponding $T_B(0)$ for at least two points at differing temperature. Ideally, these data consist of a set of approximately five data points covering as wide a temperature range as possible. Figure 1 indicates how $T_B(h)$ and $T_B(0)$ could be obtained for a number of different temperatures.

The input data necessary to calculate W_s, the sky radiance term, comes from the solution of Equation 19, requiring $T_B(h, 0)$ and $T_B(h,\theta)$ as inputs. These values are the apparent temperature observed at the same point through two look angles where one look angle is chosen as zero degrees for convenience. (Note also that Equation 11 can be solved directly for W_s, i.e., a one point solution is available). The minimum data required to solve Equation 19 consist of two data sets composed of $T_B(h,0)$ and $T_B(h,\theta)$ for two distinct points. In general, a number of points with a large range in temperature should be used to solve for m and I in Equation 19. This data set can be collected by flying two parallel flight lines and allowing for some sidelap. This procedure is often used to obtain complete target coverage and would add little or no time to most collection efforts. Figure 2 illustrates how these data could be obtained.

A ground-truth program was used to evaluate these radiometric calibration techniques. This, effort involved aerial overflights of a boat anchored at a series of positions in the Hudson River, both within and beyond the thermal plumes of various power plants.

With the boat anchored at a given position, readings were made on the upstream (downstream if flow was upstream in the estuary) side of the boat. Measurements consisted of temperatures recorded from a submerged thermistor (nominally at a depth of 6 in.) and from a Barnes PRT-5 radiometer. During each fly-over, approximately ten readings were recorded and averaged to predict the temperature at a point. To insure unbiased data, all surface measurements were made by independent consultants and surface data were withheld until aerial results had been delivered to the New York State Energy Research and Development Authority (NYSERDA). The surface radiometer was calibrated in the field under prevailing atmospheric conditions to ensure that all measurements were absolute surface temperature measurements.

The main survey took place on September 24, 1976 with the boat anchoring at eight positions throughout the day. The aircraft flew over each position four times, permitting 32 data-comparison points for the total survey. Because the boat was covered with aluminum foil, it had a low emissivity and could be located as a "cold" spot on the image. Surface temperatures were predicted using the calibration technique discussed above. Data were also collected at eight positions for five overflights on both July 8 and 9, 1976. However, the July 8 data could not be used because of calibration problems with the surface instrument.
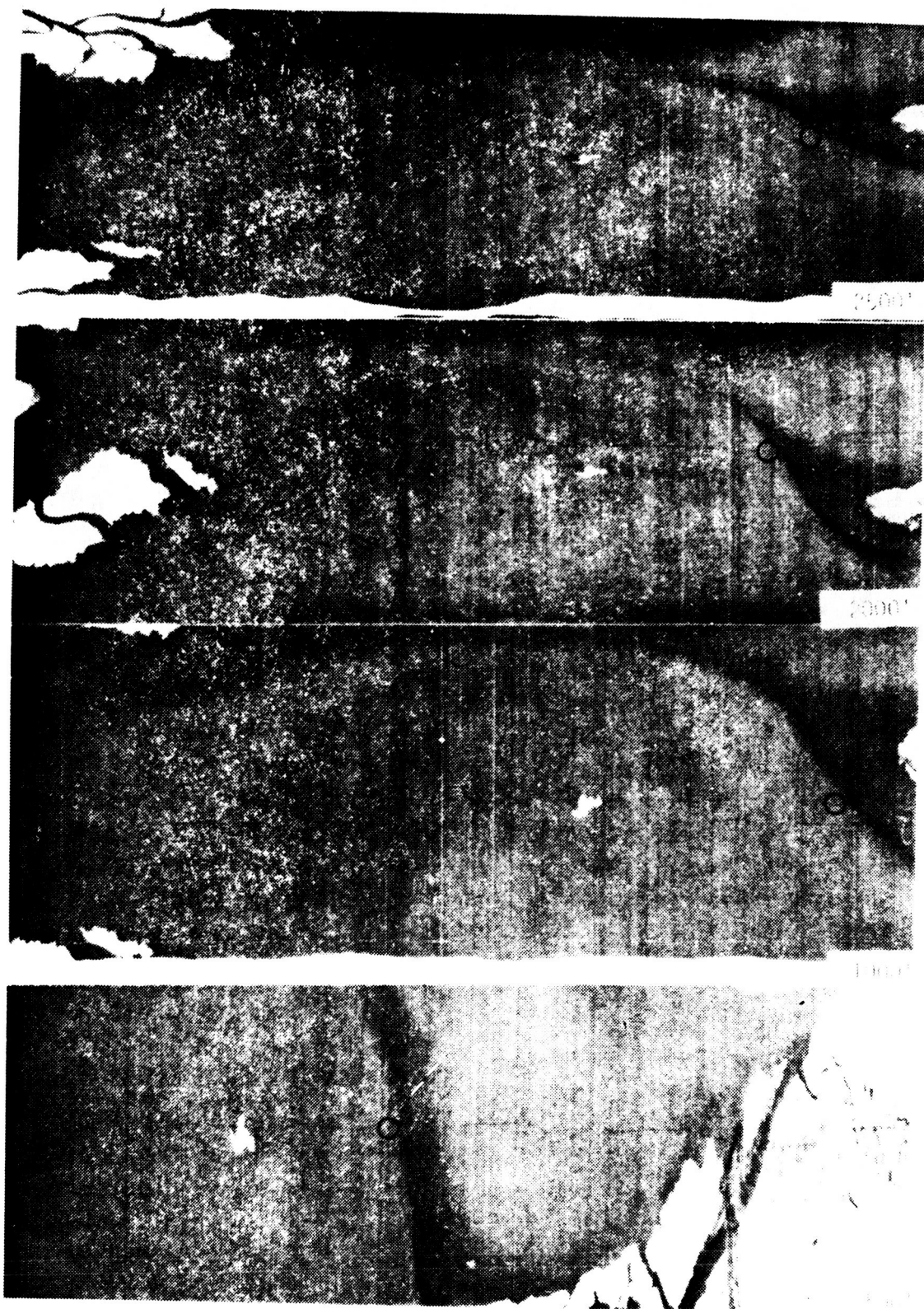
FIG. 1. Thermal images obtained during a profile. Areas of equal temperature where apparent temperature readings could be made are indicated.
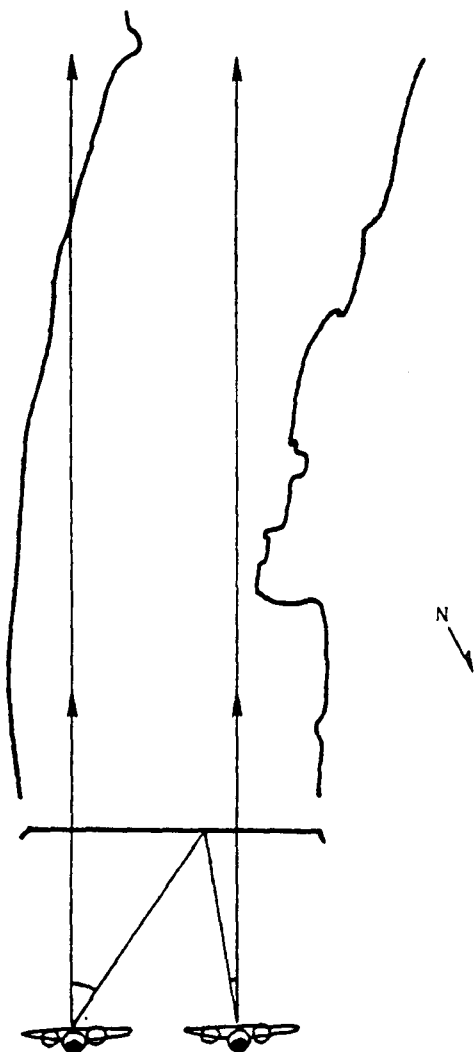
Fig. 2. Example of parallel flight lines over a power station showing the change in look angle for a given ground point.

Results

Table 1 presents the results of the data correlation for September 24. The mean and standard deviations of the absolute value of the difference between the aerial and surface data are presented. Radiometric surface data were used because they are a more accurate measure of the actual surface temperatures than is the submerged thermistor.

Comparison of submerged (6 in.) thermistor data and aerial data showed a mean difference of 0.51°F with a standard deviation of ±0.46°F. Also included is a correlation of radiometric temperatures, to which no atmospheric correlations have been applied, with the surface data. Table 2 contains the results of the July 9 survey.

When the July and September data are combined, a mean error of 0.70°F is obtained with a standard deviation of ±0.59°F (Angular Technique). This compares with a mean error of 3.23°F with a standard deviation of ±1.25°F if only internal system calibration is used. Figure 3 illustrates the precision of the calibration technique and the limitations of using only internal scanner calibration. The figure shows the surface radiometer data plotted against the calibrated (*) and uncalibrated (□) scanner data. The data, which have been corrected for atmospheric and background effects, show a very close fit within the 1°F error bars. The data using only the internal scanner calibration show sizable errors and are generally less than the actual temperature. Note that this is generally the case but that a temperature higher than the true surface temperature can be detected by airborne systems under certain atmospheric and background conditions.

One shortcoming to the angular technique is a requirement for extra data to permit calibration and some additional data processing. Neither the time nor the cost is appreciable; however, the data must be properly collected. Some improvements in accuracy could be expected if data collection were modified to facilitate analysis using the angular technique. Major improvements cannot be expected because temperatures predicted from the air approach the accuracies obtainable by surface measurements.

Conclusions and Recommendations

The data correlation results presented in the previous section indicate that a major advance in airborne radiometric measurement of water surface temperatures has been achieved.[*] Measurement accuracies essen-

TABLE 1. COMPARISON OF SURFACE AND AERIAL DATA FOR 24 SEPTEMBER 1976 (°F)

	Surface Radiometer and Uncorrected Airborne Scanner	Surface Radiometer and Angular Technique
Mean of the absolute value of the temperature difference between boat and aircraft.	4.19	0.55
Standard deviation of ΔT	±1.22	±0.57

TABLE 2. COMPARISON OF SURFACE AND AERIAL DATA FOR JULY 9, 1976 (°F)

	Surface Radiometer and Uncorrected Airborne Scanner	Surface Radiometer and Angular Technique
Mean of the absolute value of the temperature difference between boat and aircraft	2.66	0.80
Standard deviation of ΔT	±1.27	±0.57

tially as good as surface measurements are demonstrated.

The data collection procedures involve only minor variations in standard collection practices requiring approximately 15 additional minutes of flight time. All data processing can be done on a desk-top computer.

The net result of these conclusions is that a fully airborne approach to measure water surface temperatures, with accuracies comparable to those obtained from surface measurements, is an operational possibility. In addition, these results were obtained through use of an outside consultant for acquisition of ground-truth data, thus precluding any bias.

We recommend that future efforts in this area be directed at techniques to generate thermal maps with appropriate corrections at angles away from vertical. The corrections developed using the angular calibration techniques are quite accurate and should be applied in map generation. Current mapping techniques do not apply a correction for variations in apparent temperature at non-vertical look angles; development of these corrective procedures in the map-generation process would allow the full accuracies developed in the angular calibration technique to be carried through to a final map product. In addition, data collected specifically for analysis using this technique should eliminate the need for iterative solutions and should further improve calibration accuracies. While major improvements in water temperature measurements could not be expected because the current results already so closely approach surface measurements, improvements applicable to such problems as a quantitative measurement of heat loss from buildings could be expected. In fact, a major advantage of this technique is that it includes consideration of sufficient variables
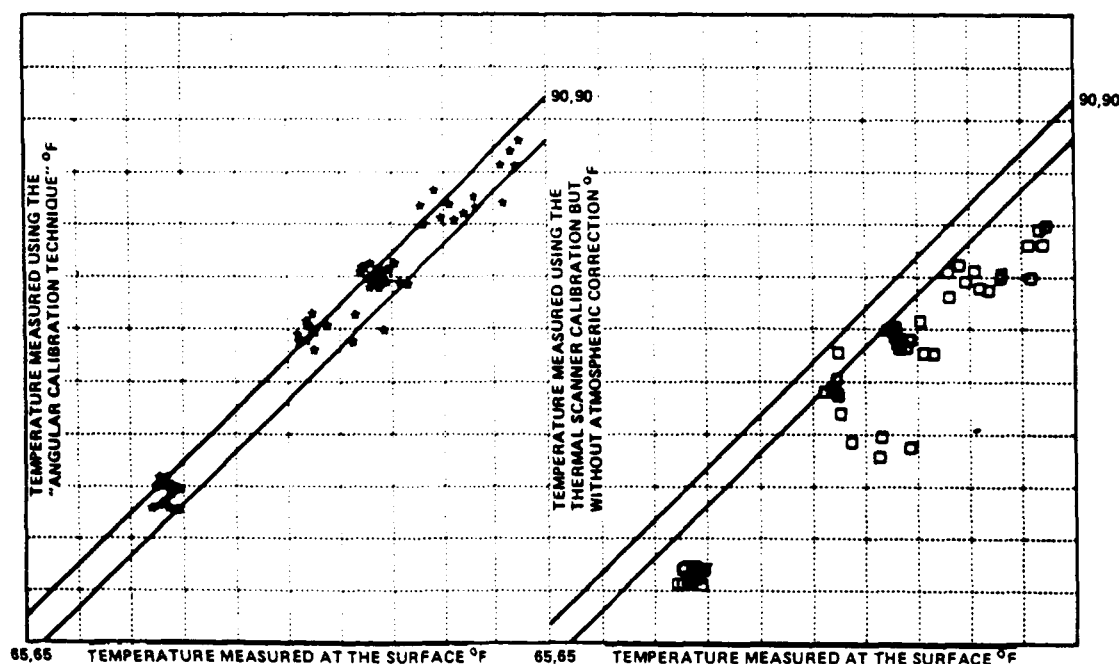

FIG. 3. Comparison of surface and aerial temperature measurements (the lines represent a 1°F error envelope).

to allow surface temperature measurement of any uniform flat surface whose emissivity is known.

REFERENCES

1. Bartolucci-Castedo, L. A., et al., *Computer Aided Processing of Remotely Sensed Data for Temperature Mapping of Surface Water from Aircraft Altitudes*, LARS Publication, Purdue University, Indiana, 1973.

2. Haynes, R. B., and J. Whipple, *Problems in Applying Infrared Reconnaissance Technology to Water Temperature Surveillance*, Technical Memorandum No. RADC/IR/TM-71-2, 1971.

3. Scapace, F. L., R. P. Madding, and T. Green III, *Scanning Thermal Plumes*, Ninth International Symposium on Remote Sensing of Environment, April 1974.

4. Schott, J. R., *Thermal Remote Sensing Calibration Techniques*, Calspan Report NA-6019-M-1, NTIS #TB-269-471, 1977.

5. *Report of Infrared Water Temperature Measurements Made September 24, 1976 of the Hudson River*, Wormser Scientific Co. Report, Stamford, Connecticut.

6. Pivovonsky, M., and M. R. Nagel, *Tables of Black Body Radiation Functions*, The Mac-Millan Company, New York 1961.

7. Schott, J. R., and R. H. Tourin, "A Completely Airborne Calibration of Aerial Infrared Water Temperature Measurements," *Proceedings ERIM Tenth International Symposium on Remote Sensing of Environment*.

8. Schott, J. R., and T. W. Gallagher, "Profile Technique For Calibration of Infrared Thermal Imaging Systems" U.S. Patent 3,970,848 July 20, 1976.

APPENDIX B

FLIGHT LOGS
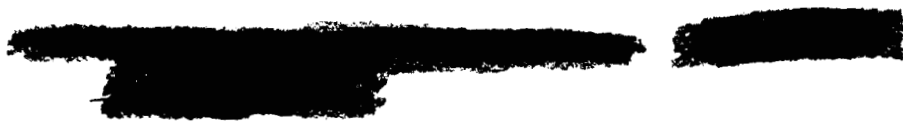
RUSSELL POWER PLANT

May 24, 1985

Time	Gain	DC	BB 8-14 m	MK	Alt
1049	54	55	9-432	1	1,000
1057				2	500
1059				3	100
1103				4	2,500
1106				5	2,500 offset
1112		Thermal Bar in		6	5,000
1120				7	10,000
1127				8	10,000 offset
1140				9	15,000
1146		Tape Jammed		10	15,000 offset
1202	140	55	Narrow Filter	11	15,000

Signal/Noise is bad

Terminate Narrowband Data

NASA
6 October '84

Target: Ginna Station
Take-Off: 0850
Land: 1145

Time	DC	Gain	MK	Remarks
				Wedge 0 - 6.0
9:09	55	68	1	500' 8 - 14
				Tape broke and replaced.
9:21			2	500'
9:23				100'
			3	1,000'
9:29			4	1,000' offset
9:37			5	5,000'
9:41			6	5,000' offset 2°C
9:51			7	10,000'
9:56			8	10,000' offset 0°C
10:08			9	15,000'
10:15			10	15,000' offset
				Tape may not be recording on Track 3.
				Switch to Track 1.
10:28			11	20,000' -19°C
10:34			12	20,000' offset Tape Rev
10:44	55	180	13	20,000' 10 - 12
		160	14	15,000'
11:04			15	10,000'
11:17			16	5,000'
11:26			17	1,000'
11:30			18	500'
				Wedge

JOHN10
TG/cs

Target: Russel Station
Take-Off: 0845

Gain	DC	BB	Mk	Alt.	Temp	Time
85	55	9-230	1	100	60°	9:02
			2	500	60°	9:06
			3	1,000	60°	
			4	1,000 off		9:17
			5	5,000	48°	9:24
			6	5,000 off		
			7	10,000	35°	9:38
			8	10,000 off		
			9	15,000	25°	9:50
			10	15,000 off		

Signal loss at end of 1,500 offset.

Wedge at both ends.

TG/cs

APPENDIX C

TM 5 RAW DATA

Data for Analysis of 6/22/84 Data Set Model Parameters

From Atmospheric Propagation Analysis

τ = 0.7929
L_u = 0.03176 x 10^{-2} w/cm²sr
L_D = 0.0385675 x 10^{-2} w/cm²srm
ε = 0.986

From Regression of L_s vs. L_g
τ = 0.8877
L_u = 0.01747 x 10^{-2} w/cm²sr

Digital Count DC	Spectral Radiance at Sensor L [mw/cm²sr μm]	Apparent Temperature at Sensor [K]	Integrated Radiance at Sensor L_s [mw/cm²sr]	Integrated Radiance at Ground L_g [mw/cm²sr]	T Predicted by Satellite [K]	T Measured by Profile [K]
128	0.847	294.07	1.750	1.826	296.95	294.77
119	0.796	289.89	1.644	1.690	291.70	290.84
129	0.854	294.66	1.766	1.846	297.68	294.77
156	1.002	305.87	2.072	2.237	311.55	311.42
139	0.908	298.86	1.877	1.988	302.90	303.89
131	0.862	295.25	1.781	1.865	298.42	295.21
130	0.858	294.97	1.774	1.856	298.07	297.39
116	0.777	288.31	1.605	1.639	289.72	289.23
176	1.118	314.05	2.312	2.544	321.55	312.77
155	1.000	305.75	2.068	2.232	311.40	308.04
163	1.044	308.91	2.159	2.349	315.28	310.75
131	0.863	295.37	1.784	1.869	298.57	298.26
127	0.839	293.44	1.734	1.805	296.16	292.57
117	0.782	288.79	1.616	1.654	290.31	290.20
127	0.841	293.62	1.739	1.811	296.38	295.21
126	0.836	293.17	1.727	1.796	295.82	294.33
160	1.024	307.50	2.118	2.296	313.55	308.72
120	0.799	290.19	1.651	1.699	292.08	293.01
141	0.917	299.57	1.896	2.013	303.78	308.04
133	0.872	296.08	1.803	1.893	299.45	296.08

Data for Analysis of 10/6/84 Data Set Model Parameters

τ = 0.78
L_u = .00341 w/cm^{2}sr
L_D = .00082 w/cm^{2}sr
ε = .986

Digital Count DC	Spectral Radiance at Sensor L [mw/cm^{2}sr μm]	Apparent Temperature at Sensor [K]	Integrated Radiance at Sensor L$_s$[mw/cm^{2}sr]	Integrated Radiance at Ground L$_g$[mw/cm^{2}sr]	T Predicted by Satellite [K]	T Measured by Profile [K]
111	0.748	285.93	1.546	1.569	286.87	294.30
125	0.827	292.49	1.710	1.748	293.97	298.50

Data for Analysis of 5/24/85 Data Set Model Parameters

From Atmospheric Propagation Analysis

$\tau = 0.85$
$L_u = 0.00023$ w/cm^{2}sr
$L_D = 0.000257145$ w/cm^{2}sr
$\varepsilon_D = 0.986$

From Regression of L_s vs. L_g
$\tau = 0.8043$
$L_u = 0.0003258$ w/cm^{2}sr

Digital Count DC	Spectral Radiance at Sensor L [mw/cm^{2}sr µm]	Apparent Temperature at Sensor [K]	Integrated Radiance at Sensor L_s [mw/cm^{2}sr]	Integrated Radiance at Ground L_g [mw/cm^{2}sr]	T Predicted by Satellite [K]	T Measured by Profile [K]
162	1.036	308.31	2.037	2.152	311.94	309.72
170	1.081	311.50	2.117	2.247	315.15	314.08
132	0.867	295.63	1.717	1.770	297.72	295.85
123	0.816	291.57	1.616	1.650	292.94	291.61
111	0.748	285.93	1.482	1.489	286.26	285.56
125	0.827	292.49	1.638	1.676	294.02	293.74
156	1.002	305.87	1.985	2.090	311.15	311.91
135	0.884	296.96	1.750	1.810	299.28	298.64
167	1.064	310.31	2.024	2.136	311.74	318.71
141	0.917	299.57	1.817	1.890	302.33	301.63
111	0.748	285.93	1.482	1.489	286.26	283.18
106	0.720	283.50	1.426	1,423	283.36	280.74
92	0.641	276.37	1.270	1.236	274.79	276.67